Published in final edited form as:
J Comput Phys. 2013 December 1; 254: . doi:10.1016/j.jcp.2013.07.033.

A novel multiblock immersed boundary method for large eddy simulation of complex arterial hemodynamics

Kameswararao Anupindi, **Yann Delorme**, **Dinesh A. Shetty**[**], and **Steven H. Frankel**[**]
School of Mechanical Engineering, Purdue University, West Lafayette, IN 47907, USA

Abstract

Computational fluid dynamics (CFD) simulations are becoming a reliable tool to understand hemodynamics, disease progression in pathological blood vessels and to predict medical device performance. Immersed boundary method (IBM) emerged as an attractive methodology because of its ability to efficiently handle complex moving and rotating geometries on structured grids. However, its application to study blood flow in complex, branching, patient-specific anatomies is scarce. This is because of the dominance of grid nodes in the exterior of the fluid domain over the useful grid nodes in the interior, rendering an inevitable memory and computational overhead. In order to alleviate this problem, we propose a novel multiblock based IBM that preserves the simplicity and effectiveness of the IBM on structured Cartesian meshes and enables handling of complex, anatomical geometries at a reduced memory overhead by minimizing the grid nodes in the exterior of the fluid domain. As pathological and medical device hemodynamics often involve complex, unsteady transitional or turbulent flow fields, a scale resolving turbulence model such as large eddy simulation (LES) is used in the present work. The proposed solver (here after referred as *WenoHemo*), is developed by enhancing an existing in-house high order incompressible flow solver that was previously validated for its numerics and several LES models by Shetty et al. [Journal of Computational Physics 2010; 229 (23), 8802-8822]. In the present work, *WenoHemo* is systematically validated for additional numerics introduced, such as IBM and the multiblock approach, by simulating laminar flow over a sphere and laminar flow over a backward facing step respectively. Then, we validate the entire solver methodology by simulating laminar and transitional flow in abdominal aortic aneurysm (AAA). Finally, we perform blood flow simulations in the challenging clinically relevant thoracic aortic aneurysm (TAA), to gain insights into the type of fluid flow patterns that exist in pathological blood vessels. Results obtained from the TAA simulations reveal complex vortical and unsteady flow fields that need to be considered in designing and implanting medical devices such as stent grafts.

Keywords

Large-eddy simulation; WENO; Multiblock; Immersed boundary method; High-order finite difference; Incompressible; Biomechanical flows

Correspondence to: Kameswararao Anupindi; Yann Delorme.
[**]Current address: Halliburton, 2107 CityWest Blvd Bldg 2, Houston, TX, 77042-2827 kamesh.a@gmail.com (Kameswararao Anupindi)

1. Introduction

Aortic aneurysm is a local permanent ballooning of the blood filled aorta [20], and is prone to rupture if not treated. Developing reliable rupture risk prediction tools is clinically important to make better aneurysm repair decisions. Knowledge of hemodynamics helps in understanding the factors that lead to initiation and growth of aneurysms. Atherosclerosis, a cardiovascular disease is the primary cause of heart disease and localization of atherosclerosis was shown to be correlated to regions of disturbed flow fields [31]. It was shown that, recirculation zone formed inside the aneurysm promotes thrombus formation and rupture [3]. Computational fluid dynamics (CFD) simulations are becoming a reliable tool to not only understand disease progression in pathological blood vessels, but also design and gauge the performance of several medical device solutions, such as stent grafts and ventricle assist devices [18, 8]. Pathological and medical device hemodynamics often involve, transitional or mildly turbulent unsteady disturbed flows with streamline curvature and rotation [37, 38]. In order to accurately simulate such flows, a scale resolving turbulence model such as large eddy simulation (LES) is required.

Turbulence modeling based on LES further requires that high order (greater than 2^{nd} order) methods be used for discretizing and solving the governing equations numerically. However, usage of high order numerical methods often limits one to use structured grids, which may not be able to handle a variety of complex geometries that arise in arterial flow domains. Immersed boundary method (IBM) emerged as an attractive methodology because of its ability to efficiently handle complex moving and rotating geometries on structured grids. The tedious job of mesh generation for complex flow domains is by-passed in these methods by constructing a global domain containing both the solid and fluid regions. IBM was introduced by Peskin [26], in which the flow field is solved on a Eulerian mesh and the immersed surface is discretized using Lagrangian points and the method was applied to the two-dimensional simulation of flow around a natural mitral valve. IBM simulations can handle moving or deforming bodies with complex surface geometry relatively easily without the need for re-meshing at every time step of the flow simulation as is needed in conventional body-fitted mesh simulations. There have been many works by several authors, in applying IBM to various fluid mechanics problems such as dragonfly flight aerodynamics [23], fish swimming [23, 11], human walking as an application of multiple moving immersed objects [5], blood flow in heart [25], fluid-structure interaction of aortic heart valve [21] and turbo machinery [29], to name a few. Certainly, the application list mentioned here is incomplete and the reader is referred to the articles by Mittal et al. [24] and by Peskin et al. [27] to gain a complete insight. Simulations based on IBM can be readily applied to external aerodynamics problems [6, 28] where the volume of the solid region is much smaller compared to the fluid region thereby reducing the amount of unnecessary grid. Adaptive mesh refinement (AMR) was used by Vanella et al. [36] as a way of reducing the amount of un-necessary grid and also to increase the resolution only in the regions of interest. Griffith et al. [12] also employed an adaptive, second order accurate IBM to simulate blood flow in heart and great vessels. They achieved enhanced boundary layer resolution in model heart valve by using locally refined mesh methodology. Using AMR one can specifically refine the mesh based on geometric or solution driven parameters.

Although IBM based simulations are quite successful in external aerodynamics problems [24, 5, 6, 28], their applications to internal fluid flow in complex geometries such as blood flow in arteries are scarce. Yokoi et al. [43] used a Cartesian grid approach together with IBM and simulated blood flow in a cerebral artery with multiple aneurysms. They used a 0.6 million Cartesian grid to immerse the cerebral artery. Although, no mention of the percentage of total grid nodes in the fluid region is made in their article, given the ratio of the diameter of the cerebral artery to its lateral extents it is apparent that a large portion of grid nodes were in the exterior of the fluid domain. Delorme et al. [8] performed LES studies of powered Fontan hemodynamics with relatively short vena cavae and long pulmonary arteries in order to reduce the amount of grid nodes lying in the exterior of the fluid domain. However, again given the longitudinal and lateral extents of the total cavopulmonary connection (TCPC) compared to its internal diameter a significant number of grid nodes were located outside of the fluid domain, as was reported in their article. These are few examples of the short comings of IBM directly applied to simulate complex arterial networks. Recently, in an effort to extend IBM to simulate complex arterial geometries, de Zélicourt et al. [7] developed a serial flow solver, using an unstructured Cartesian grid approach and studied blood flow in a real-life TCPC anatomy. As de Zélicourt et al. [7] point out in their article, one possible reason for the scarcity of studies on IBM applied to study blood flow in complex internal flow configurations, could be because of the prohibitive memory and computational demands on the single block grids that arise in order to handle these geometry. Another point that is of concern in handling complex geometries on structured grids is the constraint that all the inflow and outflow boundaries of the geometry have to terminate only on the boundary faces of the global bounding box that encloses both the fluid and solid regions. This requirement could be met in certain cases (as was done in Yokoi et al. [43] and Delorme et al. [8]) by properly truncating the complex geometry and in some cases it is not possible. Such alterations of the complex geometry to make it compatible for single block simulations might result in altering the results obtained compared to the unaltered geometry and sometimes the inflow boundary conditions may not even be known at the altered locations. In order to overcome the aforementioned problems and extend the applicability of IBM to simulate blood flow in complex anatomies, we propose a method based on a combination of multiblock structured grids and IBM on an inherently parallel framework. This particular methodology not only enables simulation of fluid flow in complex geometries but also reduces the amount of un-necessary grid that goes into the solid regions.

The organization of the paper is as follows. In sections 2 and 3 we present the governing equations, the mirroring immersed boundary method developed by Mark et al. [22] and the multiblock methodology employed in the present work. In section 4, we perform simulations using *WenoHemo* for three-dimensional laminar flow over a sphere and laminar flow over a backward facing step which validates the IBM and multiblock approaches respectively. Then we validate the combined solver by simulating the laminar and transitional flow in abdominal aortic aneurysm (AAA) and compare them to the experimental results of Asbury et al. [1]. Then we study blood flow in thoracic aortic aneurysm (TAA) which establishes the applicability of the proposed solver to complex arterial geometries.

2. Governing Equations

The governing equations for the present problem are the incompressible Navier-Stokes equations. In LES, these are filtered using a low-pass spatial filter and they are summarized below in non-dimensional form:

$$\frac{\partial \overline{u_i}}{\partial t}+\overline{u_j}\frac{\partial \overline{u_i}}{\partial x_j}=-\frac{\partial \overline{p}}{\partial x_i}+\frac{1}{Re}\frac{\partial^2 \overline{u_i}}{\partial x_j \partial x_j}-\frac{\partial \tau_{ij}}{\partial x_j} \quad (1)$$

$$\frac{\partial \overline{u_i}}{\partial x_i}=0 \quad (2)$$

where u_i is the i^{th} component of velocity vector, p is the fluid pressure, τ_{ij} is the sub-grid scale (SGS) stress tensor, Re is the Reynolds number and overbar on the variables denotes filtering operation in the equations (1, 2). The SGS stress tensor τ_{ij} shown in the equation (1), represents the difference between filtered velocity product and the product of filtered velocities given by

$$\tau_{ij}=\overline{u_i\, u_j}-\overline{u_i}\,\overline{u_j} \quad (3)$$

2.1. Sub-grid Scale Modeling

The SGS stress tensor shown above in equation (3), needs to be modeled to close the filtered Navier-Stokes equations (1). The classical eddy-viscosity model which employs Boussinesq hypothesis that relates the SGS stress tensor (τ_{ij}) to the filtered strain rate tensor can be written as follows:

$$\tau_{ij}=-2\nu_t\,\overline{S_{ij}}, \quad (4)$$

where ν_t is the turbulent eddy viscosity, in the present case also known as the SGS eddy viscosity and $\overline{S_{ij}}=\frac{1}{2}(\frac{\partial\overline{u_i}}{\partial x_j}+\frac{\partial\overline{u_j}}{\partial x_i})$ is the filtered strain rate tensor. Next, we need to determine the value of the SGS eddy viscosity (ν_t) and how this is calculated defines different types of eddy viscosity based models. In the present work, we use Vreman SGS model [39], that is a global coefficient eddy viscosity model and applicable to fully in-homogeneous flows [39, 33]. The eddy viscosity in this model is computed as follows:

$$\nu_t=C\Pi^g, \quad (5)$$

where

$$\Pi^g=\sqrt{\frac{B_\beta}{\alpha_{ij}\,\alpha_{ij}}}, \quad (6)$$

$$\alpha_{ij}=\frac{\partial\overline{u}_j}{\partial x_i}, \quad (7)$$

$$\beta_{ij}=\Delta_m^2\,\alpha_{mi}\,\alpha_{mj}, \quad (8)$$

$$B_\beta=\beta_{11}\,\beta_{22}-\beta_{12}^2+\beta_{11}\,\beta_{33}-\beta_{13}^2+\beta_{22}\,\beta_{33}-\beta_{23}^2. \quad (9)$$

In the present study, the global coefficient of the Vreman model, C, is taken equal to 0.07. Further details and validation of the model can be found in the original article by Vreman [39].

3. Computational Method

In the present work, a high order accurate incompressible fluid flow solver (*WenoHemo*) previously developed and validated for fully in-homogeneous turbulent flows by Shetty et al. [33], is augmented with mirroring IBM developed by Mark et al. [22] and a novel multiblock approach to handle fluid flows arising in complex geometries. The numerical methods employed in *WenoHemo* is discussed here briefly, for a detailed discussion the readers are referred to the article by Shetty et al. [33].

The convective acceleration terms are discretized using a 5^{th}-order accurate weighted essentially non-oscillatory scheme (WENO) [15], and the viscous terms are discretized using the standard 4^{th}-order central difference scheme. The governing equations are integrated using a fractional step method, in which a predictor-corrector algorithm [33] is employed on a staggered Cartesian grid. The velocity values are predicted without considering the pressure gradient terms and a pressure Poisson equation is solved in the corrector step to satisfy the divergence free condition of the velocity. The obtained pressure field is then used to correct the velocities that were computed in the predictor step. The time advancement is carried out using explicit 3^{rd} order accurate difference formulas described in Shetty et al. [32]. The pressure Poisson equation was solved using MUDPACK libraries in the previous single block version of the code, in the present multiblock code, this is replaced with *hypre* [10, 13] library, which solves the elliptic equations on a distributed memory machine using message passing interface (MPI) library. The tool set provided by *hypre* consists of a wide variety of fast iterative solvers that scale well in parallel.

3.1. Mirroring Immersed Boundary Method

For the sake of completeness, here we describe the working details of mirroring IBM that was proposed and tested by Mark et al. [22] for incompressible flow simulations. The same method was also tested by Chaudhuri et al. [4] for compressible flow simulations with shocks. In the IBM, a Lagrangian surface mesh of the immersed boundary is used to demarcate the solid and fluid regions on the Eulerian mesh which happens to be the domain on which the governing equations (1) are solved. Identification of inside/outside of a surface is known as a *point in polyhedron* problem in computer graphics and in the present work we make use of the algorithm described by Choi et al. [5]. A function known as a level set was constructed from the algorithm described in Choi et al. [5]. The level set function (φ) assumes values as follows:

$$\phi=0 \quad on \quad \Gamma_{IB} \qquad (10)$$

$$\phi>0 \quad in \quad \Omega_{FLUID} \qquad (11)$$

$$\phi<0 \quad in \quad \Omega_{SOLID} \qquad (12)$$

where Ω_{FLUID} indicates the fluid domain, Ω_{SOLID} represents the solid domain and Γ_{IB} demarcates the fluid domain from the solid domain and serves as the Lagrangian immersed boundary. To compute the level set function, each Eulerian mesh point has to be compared with all the Lagrangian mesh points and this becomes a slow process as the number of Eulerian mesh points increase. In order to speed up the level set computation considerably we make use of kd-tree based searching algorithm as described in Kennel [17]. The search algorithm used in kd-data structure is a generalization of the binary search tree to higher dimensional spaces. Using the kd-tree search algorithm one can locate the closest neighbor to a chosen vector in only $O(logN)$ time instead of the linear search that requires $O(N)$ time, with N being the number of degrees of freedom of the Lagrangian mesh. The Fortran95 version of the open source package KDTREE2 developed by Kennel [17] is used in the present work and the same is available for download from [17].

The immersed body was meshed with triangular elements by using the commercial mesh generation package GAMBIT, produced by ANSYS Inc. Then this surface mesh description was read by the *WenoHemo* solver, to compute the level set function. As described in Chaudhuri et al. [4], a mapping function is defined based on the values of the level set function as follows:

$$\zeta_{ijk}=0 \quad if\, \phi<0 \quad (13)$$

$$\zeta_{ijk}=1 \quad if\, \phi \geq 0 \quad (14)$$

Next, we identify the ghost points (GP), boundary points (BP) and image points (IP), surrounding the immersed boundary points. Both the mapping function, as well as GP, BP, IP are identified for each velocity component on the staggered grid. Let Γ be the set consisting of GP, BP and IP. Ghost points are defined as the points in the solid region (Ω_{SOLID}) that have at least one fluid neighbor or near neighbor as defined in equations (15,16). The inclusion of near neighbor points is required by the WENO scheme stencil, so that at least two ghost point layers are marked inside the solid region, surrounding the IB [4]. This is the only thing to be ensured while using WENO scheme with the IBM methodology and no other changes needs to be done in the implementation of the WENO scheme near the immersed boundary. The ghost points are computed along all three coordinate directions and stored in the set Γ as follows:

$$\Gamma_{GP}=(x_i,y_j,z_k) \in \Omega_{SOLID} \;\; if \;\; \exists \;\; (x_l,y_m,k_n) \; \in \; \Omega_{FLUID} \;\; for \quad (15)$$

$$l=i-2,\ldots,i+2; m=j-2,\ldots,j+2; n=k-2,\ldots,k+2 \quad (16)$$

Once GP are marked, their corresponding BP and IP need to be identified. The BP are located on the IB and IP are located in the fluid region being a mirror image of the GP about the Lagrangian mesh face normal. Figure 1 shows the schematic of a triangular face from the Lagrangian mesh and the set of three points GP, BP and IP identified on it. The GPs are always located on the Eulerian mesh, but the IPs may or may not be located on the Eulerian mesh. Hence, the primitive variables at the IPs are interpolated from the grid points that form a bounding box enclosing the IP. A tri-linear interpolation is performed to obtain the staggered velocity values in each direction at the IP. Staggered velocity values at each GP ($\overline{u}_i^{GP}$) are then assigned before calling the predictor step, as follows:

$$\overline{u}_i^{GP}=2\overline{u}_i^{BP}-\overline{u}_i^{IP}, \quad (17)$$

where $\overline{u}_i^{BP}$ is the target value of velocity vector on the IB and $\overline{u}_i^{IP}$ is computed using tri-linear interpolation. After the predictor step the velocities predicted in the solid region are nullified before feeding the velocity field to the pressure Poisson solver as described in Mark et al. [22], so as to maintain mass conservation and homogeneous Neumann pressure boundary condition across the IB.

3.2. Multiblock methodology

In the present work, equal blocks with uniform mesh size are utilized thus making the block interface to be conformal and no special interpolation have to be performed at the block-interfaces. These equal sized blocks are used to cover the simulation domain based on the immersed boundary geometry as the input. Special care was taken for the blocks which have inlet or outlet faces ending on them, so that they have one of the block faces to be perfectly aligned with the inlet and outlet faces of the immersed boundary. As many blocks as needed are arranged such that they entirely enclose the given immersed body. Each block is assigned to one parallel processor. In the present simulations the block sizes and positions are determined manually and fed to the code. Efforts are under progress to automate the process of block discretization for any given immersed boundary so that *WenoHemo* tool can be used quickly for other bio-medical flow applications. The superiority of the multiblock approach over the single block approach can be explained by referring to Figure 2. A schematic of TAA is shown in Figure 2. The *Inlet* face labeled in Figure 2 is where aortic valve is located through which blood is pumped by heart to the ascending aorta. The three outlets labeled as *O1, O2*, and *O3* are the brachiocephalic artery, left common carotid artery and left subclavian artery respectively that carry oxygenated blood to arms and to brain. The main outlet marked as *O4* carries blood to the abdomen.

As can be seen from Figure 2(a), single block representation of the flow domain cannot be used to simulate this problem without altering the geometry. Since the faces *Inlet* and *O4* do not terminate at one of the faces of the bounding box, they have to be either extended or truncated in order to be able to simulate using a single block grid. The results obtained from such an altered geometry may not be a true representation of the results that would be obtained by simulating the original geometry. Hence, the solver has to be augmented such that it does not alter the geometry of the complex arteries in order to solve for the fluid flow. The multiblock approach as shown in Figure 2(b) can handle all the inlet and outlet faces without altering them. This approach reduces the amount of wasted grid points (that is those mesh points lying in the Ω_{SOLID} region) Clearly, from Figure 2 we can note that

$$[\Omega_{SOLID}]_{singleblock} > \sum_{k=1}^{nb} [\Omega_{SOLID}]_k \quad (18)$$

where *nb* is the number of blocks in the multiblock case shown in Figure 2(b). Frames (c) and (d) denote multiblock decomposition with 100 and 325 processors respectively. In addition, the multiblock approach does not alter the original geometry to be simulated, thus it makes an attractive method to simulate internal fluid flows in complex geometries. In the present work only two-dimensional block/domain decomposition is used owing to the symmetry of the problems considered about one of the axis, but the methodology presented here can be extended to three-dimensional domain decomposition without any computational difficulty.

To further establish the superiority of multiblock simulation methodology over a single block simulation we consider using several multiblock arrangements that enclose the entire fluid domain to be simulated as shown in Figure 2. We consider a single block case (SB) as shown in frame (a) of the figure and three multiblock cases, MB1, MB2 and MB3 which utilize respectively 33, 100 and 325 blocks to enclose the fluid domain of interest. We then compute the number of mesh points required per block in order to maintain the same grid spacing in each direction. These values are presented in Table 1. A metric known as Volume Ratio (VR) is defined that computes the volume of the multiblock domain to the equivalent single block domain that would be required to simulate the same problem. VR directly relates to the savings in number of mesh points. As we can see from this table for the MB1 case we are simulating on a 62% of the mesh count, whereas for the MB2 case we are working on only 50% of the mesh size that would be needed for a single block simulation and finally for the MB3 case with 325 processors the blocks enclose the fluid domain very efficiently such that only 40% of the single block mesh resolution is sufficient to simulate the problem at the same grid spacing. Of course, in a limit the minimum VR that could be obtained would equal the ratio of volume of the fluid domain of interest to the volume of the single block domain. Hence, by efficiently arranging the blocks around the fluid domain we can achieve such a locally structured but globally unstructured mesh that simulates the problem at a reduced computational cost.

3.3. Solution of Poisson equation

The pressure Poisson equation that results in the fractional time step method needs be to solved at every time step of the flow simulation. This equation for pressure can be derived by by forcing the velocity field at the next time level $\overline{u}_i^{n+1}$ to be divergence free [33] and can be written as follows:

$$\nabla^2 \overline{p}^{n+1} = \frac{\nabla . \overline{u}_i}{\Delta t} \quad (19)$$

where $\bar{u}_i$ is the predicted velocity field from the velocity field at the latest available time level $\overline{u}_i^n$, Δt is the time step size, and p^{n+1} is the pressure field to be computed such that the velocity field at the next time level $(\overline{u}_i^{(n+1)})$ is divergence free. This elliptic equation is discretized in the present work using a second order central difference operator. Using this the left hand side of the equation (19), leaving the over bar and the time step level for brevity, can be written as follows:

$$\nabla^2 p_{i,j,k} = \frac{\partial^2 p}{\partial x^2} + \frac{\partial^2 p}{\partial y^2} + \frac{\partial^2 p}{\partial z^2}, \quad (20)$$

$$\frac{\partial^2 p}{\partial x^2} = \frac{p_{i+1,j,k} - 2p_{i,j,k} + p_{i-1,j,k}}{\Delta x^2}, \quad (21)$$

$$\frac{\partial^2 p}{\partial y^2} = \frac{p_{i,j+1,k} - 2p_{i,j,k} + p_{i,j-1,k}}{\Delta y^2}, \quad (22)$$

$$\frac{\partial^2 p}{\partial z^2} = \frac{p_{i,j,k+1} - 2p_{i,j,k} + p_{i,j,k-1}}{\Delta z^2}, \quad (23)$$

and similarly the right hand side of the equation, for brevity leaving the over bar that denotes filtering operation, can also be written as follows:

$$\frac{\nabla . u_i}{\Delta t} = \frac{1}{\Delta t} \left(\frac{\partial u}{\partial x} + \frac{\partial \upsilon}{\partial y} + \frac{\partial w}{\partial z} \right), \quad (24)$$

$$\frac{\partial u}{\partial x} = \frac{u_{i+1/2,j,k} - u_{i-1/2,j,k}}{\Delta x}, \quad (25)$$

$$\frac{\partial \upsilon}{\partial y} = \frac{\upsilon_{i,j+1/2,k} - \upsilon_{i,j-1/2,k}}{\Delta y}, \quad (26)$$

$$\frac{\partial w}{\partial z} = \frac{w_{i,j,k+1/2} - \omega_{i,j,k-1/2}}{\Delta z} \quad (27)$$

where Δx, Δy and Δz are the grid sizes in x, y and z directions respectively. In the present work, we use the *hypre* [13, 9, 10] library to solve the Poisson equation on a multiblock grid in parallel. Preconditioned conjugate gradient (PCG) method was used with geometric multigrid as the preconditioner for solving the discretized Poisson equation as described in

Ashby et al. [2]. The convergence criterion was set to a relative tolerance of $1e - 12$ and 3 iterations of pre- and post- sweeps are performed on each multigrid level. The Dirichlet boundary conditions on pressure were symmetrized in order to form a symmetric matrix that is required for solving the system using a conjugate gradient method. Symmetrization of a matrix at grid nodes that have a Dirichlet boundary condition can be explained as follows. Let a one-dimensional grid be represented as $i = 0, 1, \ldots, N-1, N$, where $i = 0$ is the left boundary and $i = N$ is the right boundary. If a Dirichlet boundary condition is applied at grid node $i = N$, then symmetrization process transfers all the entries of the matrix at the grid node $i = N - 1$ that have coefficients associated with the known Dirichlet value at $i = N$ to the right hand side vector of the linear system.

3.4. Parallelization

The *WenoHemo* solver is parallelized using the message passing interface (MPI). MPI allows the code to be run on a distributed memory cluster which is apt for large scale computing. A sample one-dimensional decomposition of a two-dimensional domain is shown schematically in Figure 3. The horizontal and vertical arrows in Figure 3 represent the location where u and v velocity components are stored respectively. In the figure, filled circles indicate the location where pressure is stored. Each processor has a ghost layer of grid points, which store the values from the neighboring process. The ghost layers on each processor are shown by dotted lines in the Figure 3. After data exchange the ghost layers are populated with the latest values from the neighboring processor. The interior mesh points on the processor $N + 1$ and the ghost mesh points on the processor N are also marked in the Figure 3, which corresponds to one pair of data exchange between P_N and P_{N+1} processors.

In order to evaluate the parallel performance of the solver, we select a test problem of mixing layer on a cubic domain and a sample of 100 time steps are simulated. Three different grid sizes of approximately 7, 16 and 55 million points are used for estimating the speed up of the *WenoHemo* solver. Processors ranging from 32 to 256 are used for testing the cases of of 7 and 16 million grid points where as upto 1024 processors is used for testing the 55 million grid points case. The time taken by the 32 processors simulation is taken as the base line simulation to calculate the speed up. The parallel performance of the *WenoHemo* solver is shown plotted in Figure 4. Together with the three grid sizes the figure also shows the ideal speed up curve. As we can see from this figure, linear speed up is obtained for grid sizes of 7 and 16 million grid points up to a processor count of 128, beyond which they deviate from the ideal speed up curve. At a processor count of 256 the higher grid size case of 16 million points shows better speedup than the lower grid size case of 7 million points. This behavior could be due to more computations involved per processor in the former case owing to a larger grid size. Based on the same reasoning the results obtained from the largest grid size considered could also be explained. The largest grid size case of 55 million grid points shows super linear speed up till a processor count of 512, beyond which it drops to sub linear speed up. The cluster on which these simulations were performed contains Intel Xeon x5650 CPUs with 12 cores per node and 48 GB of RAM per node. The CPUs are connected through a quad data rate (QDR) InfiniBand interconnect.

4. Results

4.1. Validation

In this section, we first test the spatial order of accuracy of the overall *WenoHemo* solver followed by validating each of its primary components newly introduced in the present study. IBM and the multiblock approach are the additional numerics that were added to the code over and above the LES solver, which was validated in Shetty et al. [33]. So, in order to be confident about the results that are produced with the present solver, we first validate these two new implementations. The solver, as a whole consisting of both the methods is validated next using AAA simulations and comparisons are made to experimental results. In order to validate the IBM, we chose flow over a sphere case and to validate the multiblock approach approach, flow over a backward facing step is chosen.

4.1.1. Order of Accuracy—The spatial order of accuracy of the present LES solver without the IBM has been previously calculated and it was shown to be 5^{th} order on a periodic domain for a Taylor-Green Vortex (TGV) solution in Shetty et al. [33]. The spatial order of accuracy of the IBM was also previously evaluated by Mark et al. [22] by simulating laminar flow over a sphere and by further computing it's drag coefficient. They showed that mirroring IBM method is second order accurate from these simulations. For the sake of completeness, here we perform test of spatial order of accuracy for the developed *WenoHemo* solver using the three-dimensional TGV that evolves from an initially two-dimensional velocity and pressure fields given by:

$$u(x,y,z,t)=-\cos(kx)\sin(ky)\exp(-2k^2t/Re), \quad (28)$$

$$v(x,y,z,t)=+\sin(kx)\cos(ky)\exp(-2k^2t/Re), \quad (29)$$

$$p(x,y,z,t)=-\frac{1}{4}(\cos(kx)+\cos(ky))\exp(-4k^2t/Re); \quad (30)$$

is considered. A domain of size $[-\pi, +\pi]^3$ is considered with $k = 1$, $Re = 100$ and a time step of $\Delta t = 0.001$. In order to bring in the effect of the IBM on this flow field, a stationary sphere is placed at the origin. All the simulations are run for 100 time steps at an equal time step on grids of sizes 8^3, 16^3, 32^3, 64^3, 128^3. The result obtained on a grid size of 256^3 is considered as the base line result for calculating the error estimates. The contours of u-velocity component on the $z = 0$ plane are shown plotted in Figure 5(a). The L_2 norm of the error in the u-velocity component is shown plotted in Figure 5(b). As we can see from this figure the present solver shows second order accuracy in space owing to the inclusion of the IBM method.

4.1.2. Flow over a Sphere—To validate the IBM that was implemented into the code, we performed simulations of flow over a sphere at several Reynolds numbers. We compared the results to the numerical results obtained by Johnson et al. [16]. The diameter of the sphere (D) is taken as the length scale and the average inlet velocity is taken as the velocity scale. The domain extends $25D$ in the x direction, and $8D$ in the y and z directions. The mesh size was set as 385 grid points in the x direction, and 129 points in each of y and z directions, making a total resolution of 6.4 million points.

The length of the re-circulation bubble (L/D) formed behind the sphere and the center of the bubble (XC/D, YC/D) are compared in Figure 6. As the Reynolds number is increased from 50 to 200 all the measured quantities increase, agreeing very well with the results of Johnson et al. [16]. For all the simulations in the Reynolds number range of 50 to 200 the flow field remains steady, with attached eddies behind the sphere.

4.1.3. Flow over a Backward Facing Step—In order to validate the multiblock solver as it is without the IBM, we performed simulations of flow over a backward facing step and compared the results to those obtained by the experiments conducted by Tylli et al. [35].

Flow over backward facing step is a standard benchmark problem for testing fluid flow solvers. The geometry considered here is same as the one used in experiments by Tylli et al. [35], and a schematic together with the multiblock decomposition into 35 equal sized blocks is shown in Figure 7. The backward facing step considered here has an expansion ratio of 2 and a downstream aspect ratio of 20. The inlet channel height is chosen as the length scale and a curve fit for the laminar flow in a plane channel is used as the velocity profile at the inlet. The domain extents in the non-dimensional units are −1 to 34 in the x-direction, −0.5 to +0.5 in the y-direction in the step region and −1.5 to +0.5 in the y-direction in the channel region and −20 to +20 in the z-direction. Dirichlet velocity boundary condition is used on the inlet with a parabolic velocity profile:

$$u=\left[1-exp\left(\frac{-z-20}{0.35}\right)\right]\times\left[1-exp\left(\frac{z-20}{0.35}\right)\right]\times\left[1-4y^2\right] \quad (31)$$

No-slip wall boundary condition is used on the walls in the y and z-direction. Outflow boundary condition employing homogeneous Neumann boundary condition on all components of the velocity is used at the outlet of the domain. The simulation used 29, 29 and 241 mesh points in x, y, and z direction respectively in each block, giving a total of about 7.1 million mesh points. Simulations were performed for a Reynolds number of 648 to match with the experimental results of Tylli et al. [35]. As pointed out by Tylli et al. [35], the flow in a backward facing step at a Reynolds number of 648 has three dimensional effects because of the side walls and hence $3D$ simulations are necessary.

At a Reynolds number of 648 the flow in the backward facing step is steady and laminar but with three-dimensional effects. The axial velocity profiles (u) as a function of the channel height (y) at several streamwise locations are shown plotted in Figure 8 on the xy-plane at $z = 0$. From Figure 8, we see that the results match very well in the range $0 < x < 12$, but slight deviations are observed towards the outlet of the domain in the range $12 < x < 20$, both in the lower and upper regions of the channel. Similar behavior in the match is observed on the plane $z = 10$, as shown in Figure 9, which is located half way between the channel side wall and the center of the channel. Another comparison between the results is made on the plane $z = 18$ which is very close to the side wall of the channel. The comparison is shown plotted in Figure 10. A very good agreement in results is obtained in the range $0 < x < 8$, even in the close proximity to the side wall. The contours of u-velocity profiles are shown plotted in Figure 11, from which we can visually notice a primary and a secondary re-circulation zones, colored by negative u velocity on the bottom and top walls of channel respectively. The formation of the primary recirculation zone can be explained based on the *coanda* effect [42, 30], whereas the secondary recirculation zone formation depends on the Reynolds number considered. For low Reynolds numbers the secondary recirculation zone may not even be formed. After comparing the u-velocity profiles, we turn our attention to look at the three-dimensional effects in the backward facing step. To understand the wall jet formation, a number of w-velocity profiles are extracted and plotted as a function of y on the xz-plane at the indicated x locations in the left column of the Figure 12 (frames (a) and (c)). An interesting observation noted by Tylli et al. [35], is that, as the wall-jet develops along the span wise direction, the w-velocity profiles become self similar in the lower portion of the channel ($0 \leq (y - y_{wall})/y_{half} \leq 1$). The self similar velocity profiles are shown plotted in the right column of the Figure 12 (frames (b) and (d)). The w-velocity components are normalized by the maximum w velocity of the profile (w_{max}) and the channel height is normalized using the half width (y_{half}, which equals the distance from the wall where the w velocity becomes half of the w_{max} velocity on the decreasing part of the profile). The y_{wall} used in the normalization equals −0.15 in the present case. As we can see from the right column of the Figure 12 the velocity profiles overlap in accordance with the self similar nature in the range $0 \leq (y - y_{wall}) / y_{half} \leq 1$.

4.1.4. Steady Inflow in Abdominal Aortic Aneurysm (AAA)—In this section, we turn our focus to simulate steady inflow in AAA for which experimental results are available in the literature. The blood flow through the arterial network is remarkably stable and the arterial walls withstand the repetitive wall stress. Unfortunately, in some cases, due to disease or other complex processes, the arterial wall becomes weak and bulges out permanently forming an aneurysm [20]. Although, there are many sites at which aneurysms can form in the arterial tree, the most common are thoracic aortic aneurysms, abdominal aortic aneurysms and cerebral aneurysms. In the present section, we focus on steady inflow simulations in AAA and comparing them to the experimental results of Asbury et al. [1]. The walls of the aorta are assumed to be rigid.

The geometry of the AAA considered in the present work is taken from the experiments of Asbury et al. [1] and is shown in Figure 13(a). The inlet and outlet to the aorta have the same diameter ($d = 2r_i$), whereas the diameter of the aneurysm is denoted by D. The diameter ratio of the aneurysm $D/d = 2.75$ is considered in the present work. Two different Reynolds numbers 500 and 2600 are considered. The diameter of the inlet (d) and the average velocity at the inlet section ($\bar{U}$) are used as the length scale and the velocity scale respectively to define the Reynolds number. A parabolic inlet velocity profile is applied at the inlet of the domain, and a homogeneous Neumann boundary condition is applied to all the velocity components at the outlet of the domain. A Dirichlet boundary condition on the pressure is applied at the outlet of the domain and a homogeneous Neumann boundary condition for pressure is set on all other boundaries. Figure 13(b) shows the multiblock decomposition of the AAA geometry into 81 equal sized blocks used for the simulation. The length of the domain from inlet to outlet measures $18d$. Each block has a mesh of $24 \times 24 \times 80$ making it a total mesh resolution of 3.7 million points.

The profiles of mean axial velocity $< \bar{u} > / \bar{U}$ are shown plotted in Figure 14(a), at indicated locations along the streamwise direction of the aorta on the xy-plane, at $z = 0$, at a Reynolds number of 500. The operator <> denotes time average or mean quantity. A good match between the present simulation results and the experimental results of Asbury et al. [1] is seen from the figure. The parabolic shape of the velocity profiles is maintained similar to the experimental results throughout the abdominal aorta. The streamlines on the xy-plane at $z = 0$ are shown plotted in Figure 14(b). From Figure 14(b) the recirculating fluid in the aneurysm can be clearly noticed. The recirculating region has a center measured in the xy-plane at $(2.25r_i, 1.55r_i)$.

Next, we compare the results obtained for a Reynolds number of 2600. The profiles of mean axial velocity ($< \bar{u} > / \bar{U}$) are shown plotted in Figure 15(a) at several locations along the axis of the aorta in the xy-plane at $z = 0$. Compared to the 500 Reynolds number case, a clear recirculation zone is noticed from the Figure 15(a). A perfect match with the experimental results could not be obtained, but until $x/r_i = 4$, the peak and the qualitative behavior of the profiles is captured by the simulations. The experimental results are not quite symmetric about the $y = 0$ line. The streamlines in the xy-plane at $z = 0$ are shown plotted in Figure 15(b). The recirculating eddy seems to be more elongated and pushed towards the distal end of the aorta in this case when compared with the Reynolds number of 500 case. The center of the recirculating fluid, when measured in the xy-plane has a center at $(3.74r_i, 1.16r_i)$, which is nearer to the distal end by a value of $1.5r_i$ units and closer to the axis of the aorta by $0.4r_i$ when compared with the Reynolds number of 500 case.

The variation of turbulence intensity of the axial component of velocity, defined as $I_u = u'_{r.m.s}/\langle\overline{u}\rangle$, is compared next between the present simulations and the experiment for 2600 Reynolds number case. The axial variation of turbulence intensity I_u is shown plotted in Figure 16. As we can see from this figure the turbulence intensity increases in the distal portion of the AAA. Towards the distal end both the experimental and present simulations show a match with a value of 14% turbulence intensity, however, in the range $2 \le x/r_i \le 10$ only the upward trend is captured. This deviation could be due to differences in inlet turbulence levels between the experiments and the simulations.

4.2. Steady Inflow in Thoracic Aortic Aneurysm (TAA)

Finally, we turn to investigate steady inflow in TAA. The geometry of TAA together with a multiblock decomposition into 100 blocks is shown in Figure 17(a). The particular geometry considered here has an additional 90° bend towards the distal end when compared with typical TAA geometries that are studied in the literature [19]. The motivation behind such an additional bend is that it is supposed to create a worst case scenario with maximum loading imparted on a stent graft placed in this geometry. A bisecting plane cut of the geometry on the xy-plane at $z = 0$ is shown in Figure 17(b). In the figure, the surface marked *Inlet* is the inflow surface to the domain, through which the blood pumped by heart enters the aorta. The surfaces $O1, O2, O3$ and $O4$ indicate outlets leading to brachiocephalic artery, left common carotid artery, left subclavian artery and to abdominal aorta respectively. The diameter of aorta at the outlet $O4$ is same as at the inlet and equal to d. The outlets $O1$, $O2$ and $O3$ have a diameter of $d/4$, $d/5$ and $3d/10$ respectively. Several point probes $P1$ through $P5$ and line probes $S1$ through $S10$ are also shown marked on the central xy-plane, which enables analysis of mean and turbulent quantities.

A uniform velocity profile is applied at the inlet of the domain. The diameter at the inlet, d and the average velocity at the inlet, $\overline{V}$, are used as the length scale and the velocity scale to define the Reynolds number. An average Reynolds number of 910 and a peak Reynolds number of 3727 are identified for the present geometry, by considering the physiological wave form used by Lantz et al. [19]. At all the outlets $O1$ through $O4$ homogeneous Neumann boundary condition for velocity is applied. Pressure level is set to a Dirichlet value on the front and back faces of the bounding box in z direction and a homogeneous Neumann pressure boundary condition is applied on all other boundaries.

4.2.1. Re = 910—A multiblock domain with 100 blocks as shown in Figure 17(a) is used for the steady inflow simulations at a Reynolds number of 910. As each block is assigned to one processor, the simulations are run on 100 processors. Each block consists of 21 × 21 × 81 mesh points, making a total resolution of 3.6 million points. The contours of normalized vorticity magnitude ($|\omega| d/\overline{V}$) are shown plotted in Figure 17(c) on the central xy-plane, at $z = 0$. As the flow turns clockwise from the inlet into the aortic arch and into the aneurysm region, the inner wall boundary layer detached from the wall, whereas the outer wall boundary layer follows the outer contour without permanent separation from the wall. The outer wall boundary layer, however, slightly moves inwards at each of the 90 degrees bends in the aneurysm and descending aorta regions. A steady and laminar flow field is observed in the entire domain under steady inflow conditions at a Reynolds number of 910.

The mean velocity profiles ($\langle \bar{u} \rangle / \overline{V}$ on lines $S1$ and $S2$ and $-\langle \bar{v} \rangle / \overline{V}$ on lines $S3$ through $S10$) are shown plotted in Figure 18 on several lines indicated in Figure 17(b). An almost flat velocity profile is seen at the location $S1$, whereas reverse flow can be seen at the stations $S2$ through $S4$. The lines $S3$, $S4$ are in the aneurysm region and they have reverse flow extending to 50% of the local diameter at the location as can be seen from this figure. The peak value of the retrograde velocities at locations $S3$ and $S4$ is 20% of $\overline{V}$, whereas at the location $S5$, the retrograde velocity is less than 5% of $\bar{V}$ marking the onset of zero retrograde flow. All the sections downstream of $S5$ do not have any retrograde velocities and profiles at the locations $S8$, $S9$ and $S10$ seem to have attained a close to a fully developed flow profile.

Next, we computed wall shear stress (WSS) on the surface of the TAA at this Reynolds number, to analyze the effect of the slow moving blood flow in the recirculation regions on the wall shear stress. The methodology presented by Mark et al. [22] is used to interpolate and compute the values onto the surface mesh from the Eulerian mesh. Figure 19 shows the normalized mean WSS plotted on the surface of the TAA in two different views in frames (a) and (b). Average value obtained from the circumferential average at the inlet of the domain is used for normalizing the WSS throughout the TAA. We can see from this figure that, a peak WSS of 2.0 is noted in regions on the three separating arteries from the aortic arch. The WSS values drop to less than 50% on the inner and outer walls of the aneurysm region.

4.2.2. Re = 3727—The same 100 block configuration as shown in Figure 17(a) is used for the peak Reynolds number simulation as well, but with a refined mesh in each block with 25×25×85 points, making it a total resolution of 5.3 million mesh points. The simulation is run on 100 processors, for a non-dimensional time of 200 and turbulent statistics are collected over the last 100. A steady inflow is applied at the inlet of the domain, but unlike the average Reynolds number case, the flow is found to be unsteady in the aneurysm and descending aorta regions. The time history of normalized y-component of velocity fluctuations ($v'/\bar{V}$) at five different probe locations $P1$ through $P5$ noted in Figure 17(b), is shown plotted in Figure 20(a), which indicates the unsteady flow field in the descending aorta region. The time history of normalized v_{rms} values at the probe locations is shown plotted in Figure 20(b), which clearly shows the convergence of the root mean square (rms) quantities over the simulation time considered.

In order to identify the disturbed flow field occurring in the aneurysm region and extending through the descending aorta, we plot the normalized mean vorticity magnitude contours on the central xy-plane at $z = 0$ in Figure 21(a). From this figure, we can see that, the wall boundary layer at the outer wall rolls up similar to a mixing layer and curves down in the aneurysm region. The wall boundary layer at the inner wall, separates similar to the average Reynolds number case, but in this case additionally produces a disturbed flow field in the aneurysm and descending aorta regions as observed from the figure. To visualize the coherent structures forming in this disturbed flow field, the iso-surfaces of λ_2 [14] corresponding to a value of −2.0, colored by normalized mean vorticity magnitude are plotted in Figure 21(b). Long vortical structures emanating from the aneurysm and extending towards the distal end with length of the order of $3d$ are noted from this figure. The clinical significance of these long vortical structures needs to be understood yet.

The mean velocity and turbulent statistics in the TAA are analyzed here, similar to the average Reynolds number case by considering the data extracted on the lines $S1$ through $S10$. The normalized mean velocity profiles are shown plotted in Figure 22(a) at the indicated locations. The $\bar{u}/\bar{V}$ velocity at the locations $S1$ shows a flat profiles with no re-circulation, whereas at the location $S2$ a small retrograde flow is found from the profile. Similar to the average Reynolds number case, the profiles at the stations $S3$, $S4$ and $S5$ capture a retrograde flow, extending close to 50% of the local diameter at the stations $S3$ and $S4$, while at $S5$ the retrograde velocity is only over 25% of the local diameter. The peak values of the retrograde velocity at $S3$ and $S4$ are approximately 25% of $\bar{V}$, where as at the station $S5$ the retrograde velocity has a peak of 11% of $\bar{V}$, which is twice more than the value found in the average Reynolds number case. Further downstream, beginning with the location $S6$, no retrograde flow is found in the profiles extracted. The turbulent statistics, $u_{rms}/\bar{V}$, $\upsilon_{rms}/\bar{V}$, $w_{rms}/\bar{V}$ and normalized turbulent kinetic energy ($k/\bar{V}^2$) are shown plotted at indicated locations in Figure 22(b), (c), (d) and (e) respectively. The unsteady and the turbulence levels are not present upstream of the aneurysm, in the regions of aortic arch as seen from the locations $S1$ and $S2$ for any of the turbulent statistics. From the extracted profiles, $u_{rms}/\bar{V}$ values show a peak value of 30% at the location $S3$ and decreasing as we move downstream, reaching a value close to 25% at the locations $S4$ through $S7$ and further to 20% at the locations $S8$ through $S10$. The $\upsilon_{rms}/\bar{V}$ profiles also show a similar pattern with peak values reaching close to 25% at the locations $S3$ and $S4$ and decreasing as we move downstream to values close to 15% at the locations $S5$ through $S10$. The $w_{rms}/\bar{V}$ profiles show close to constant values with peak values reaching to 14% at the location $S3$ and decreasing only to 12% at the location $S10$. The turbulent kinetic energy profiles shown in Figure 22(e), also shows a decreasing trend as we traverse from $S3$ towards the distal end at $S10$. The peak turbulent kinetic energy ($k/\bar{V}^2$) at the location $S3$ reaches a value of 8%, decreasing to a value of 3% at the location $S10$.

In order to characterize the flow in TAA, the energy spectrum of the of the y–component of the velocity fluctuations (υ') is computed at several points ($P1$ through $P5$, shown in Figure 17(b)) in the aneurysm and in the descending aorta regions. The energy spectra obtained are shown plotted in Figure 23. The frequency spectra $E_{22}(S)$ are computed by using Welch's method [40], with no overlap. The energy spectra are plotted as a function of the Strouhal number $S = fd/\bar{V}$ where f is the frequency of eddy motions at the probe location. The lines corresponding to $S^{-5/3}$ and S^{-7} have also been shown plotted in the figure. In turbulent flows, the $S^{-5/3}$ variation in the energy spectrum is associated with the energy transfer from low wave number to high wave numbers and is dominated by inertial transfer [34]. This region is also known as inertial sub range and the process of transfer of energy is known as spectral energy cascade. The variation of S^{-7} is a characteristic of dissipation range in which viscous forces dominate [41]. From Figure 23, we can see that points $P1$, $P2$, $P4$ and $P5$ seem to have a broader range of frequencies when compared with probe $P3$, for inertial sub range, whereas at higher frequencies all the probes record viscous dissipation.

Finally, we compute the normalized WSS similar to the average Reynolds number case and is shown plotted in Figure 24 in two different views in frames (a) and (b). As we can see from this figure, the maximum WSS is 6 times the average inlet value and occurs in the distal end of the aorta. The inner and outer walls of the aneurysm region and few portions of descending aorta continue to show smaller values of WSS of the order of 0.5, similar to the average Reynolds number case, but the peak value of WSS obtained in this case is 3 times larger than the one obtained in the average Reynolds number case.

5. Conclusions

In the present work, we developed a novel method that combines a multiblock approach with the existing mirroring IBM to simulate fluid flow problems in complex arterial hemodynamics. To the authors' knowledge this is the first time such a combined method has been applied for simulating blood flow in arteries. Several validation test cases are presented to validate each of the main components of the developed *WenoHemo* solver. The overall spatial order of accuracy of the solver is shown to be second order using a TGV problem with a stationary sphere. The parallel efficiency of the solver is also evaluated and linear speed up range of the solver is identified depending on the problem size considered. The results obtained for laminar flow over a sphere, laminar flow over a backward facing step and laminar and transitional flow in AAA show good agreement to the existing numerical and experimental data. Steady inflow in TAA is studied at an average Reynolds number of 910 and a peak Reynolds number of 3727. The average Reynolds number simulation shows

NIH-PA Author Manuscript
NIH-PA Author Manuscript

a steady flow field, whereas the peak Reynolds number simulation reveals an unsteady flow field with complex vortical structures in the aneurysm and the descending aorta regions. The methodology presented here and the results obtained indicate that the proposed solver based on multiblock IBM enables efficient simulation of pathological and medical device hemodynamics in complex blood vessel anatomies using an inherently parallel framework.

Future work will focus on applying the developed multiblock *WenoHemo* code to study blood flow in TAA under pulsatile inflow conditions. Applying the present code to reevaluate the performance of viscous impeller pump in the TCPC [8] is also planned.

Acknowledgments

We would like to thank Dr. Shuo Yang and Dr. Jarin Kratzberg of MED Institute, West Lafayette, IN, for reconstructing and providing us with the TAA geometry from patient-specific magnetic resonance imaging scan. This particular geometry has motivated us to develop the present novel solver and we acknowledge the same. KA would like to thank Dr. Robert Falgout for his suggestions and help in answering his questions related to setting up and using the *hypre* [13, 2, 9, 10] software library and Prof. Charles Asbury, for his help in answering questions related to reconstructing the AAA geometry from the models used in their experiments [1]. The authors would like to acknowledge the financial support received from the collaboration between Technology Assistance Program (TAP) at Purdue University and MED Institute, West Lafayette, IN. The partial financial support received from National Institute of Health (NIH) Grant HL098353, in carrying out this work is also acknowledged. The computational resources provided through TAP on Ohio Super Computer cluster is gratefully acknowledged.

References

1. Asbury CL, Ruberti JW, Bluth EI, Peattie RA. Experimental investigation of steady flow in rigid models of abdominal aortic aneurysms. Annals of Biomedical Engineering. 1995; 23(1):29–39. URL http://www.ncbi.nlm.nih.gov/pubmed/7762880. [PubMed: 7762880]
2. Ashby SF, Falgout RD. A parallel multigrid preconditioned conjugate gradient algorithm for groundwater flow simulations. Nuclear Science and Engineering. 1996; 94551(1):145–159. URL http://www.llnl.gov/CASC/linear_solvers/pubs/ashby_falgout_pfmg.pdf.
3. Bluestein D, Niu L, Schoephoerster RT, Dewanjee MK. Steady flow in an aneurysm model: correlation between fluid dynamics and blood platelet deposition. Journal of biomechanical engineering. Aug; 1996 118(3):280–6. URL http://www.ncbi.nlm.nih.gov/pubmed/8872248. [PubMed: 8872248]
4. Chaudhuri A, Hadjadj A, Chinnayya A. On the use of immersed boundary methods for shock/obstacle interactions. Journal of Computational Physics. Mar; 2011 230(5):1731–1748. URL http://linkinghub.elsevier.com/retrieve/pii/S0021999110006248.
5. Choi J-I, Oberoi RC, Edwards JR, Rosati Ja. An immersed boundary method for complex incompressible flows. Journal of Computational Physics. Jun; 2007 224(2):757–784. URL http://linkinghub.elsevier.com/retrieve/pii/S0021999106005481.
6. Colonius T, Taira K. A fast immersed boundary method using a nullspace approach and multi-domain far-field boundary conditions. Computer Methods in Applied Mechanics and Engineering. Apr; 2008 197(25-28):2131–2146. URL http://linkinghub.elsevier.com/retrieve/pii/S0045782507003362.
7. de Zélicourt D, Ge L, Wang C, Sotiropoulos F, Gilmanov A, Yoganathan A. Flow simulations in arbitrarily complex cardiovascular anatomies – An unstructured Cartesian grid approach. Computers & Fluids. Oct; 2009 38(9):1749–1762. URL http://linkinghub.elsevier.com/retrieve/pii/S0045793009000504.
8. Delorme Y, Anupindi K, Kerlo A, Shetty D, Rodefeld M, Chen J, Frankel S. Large eddy simulation of powered fontan hemodynamics. Journal of Biomechanics. 2013; 46(2):408–422. special Issue: Biofluid Mechanics. URL http://www.sciencedirect.com/science/article/pii/S0021929012006525. [PubMed: 23177085]
9. Falgout, RD.; Jones, JE. Multigrid on Massively Parallel Architectures. In: Dick, E.; Riemslagh, K.; Vierendeels, J., editors. Multigrid Methods VI Vol 14 of Lecture Notes in Computational Science

and Engineering. Springer; 2000. p. 101-107.URL http://citeseerx.ist.psu.edu/viewdoc/summary?doi=10.1.1.42.6523

10. Falgout, RD.; Yang, UM. hypre: A library of high performance preconditioners. 2002. URL http://www.springerlink.com/index/G0FJ31WFNHCGEUBL.pdf
11. Gilmanov A, Sotiropoulos F. A hybrid Cartesian/immersed boundary method for simulating flows with 3D, geometrically complex, moving bodies. Journal of Computational Physics. 2005; 207(2): 457–492. URL http://linkinghub.elsevier.com/retrieve/pii/S0021999105000379.
12. Griffith BE, Hornung RD, Mcqueen DM, Peskin CS. An adaptive, formally second order accurate version of the immersed boundary method. Journal of Computational Physics. 2007; 223(1):10–49. URL http://linkinghub.elsevier.com/retrieve/pii/S0021999106004207.
13. Hypre, 2001. high performance preconditioners. URL http://llnl.gov/CASC/hypre
14. Jeong J, Hussain F. On the identification of a vortex. Journal of Fluid Mechanics. 1995; 285(-1): 69–94. URL http://www.journals.cambridge.org/abstract_S0022112095000462.
15. Jiang G-S, Shu C-W. Efficient implementation of weighted ENO schemes. Journal of Computational Physics. 1995; 126(1):202–228. URL http://linkinghub.elsevier.com/retrieve/pii/S0021999196901308.
16. Johnson TA, Patel VC. Flow past a sphere up to a Reynolds number of 300. Journal of Fluid Mechanics. 1999; 378(-1):19–70. URL http://www.journals.cambridge.org/abstract_S0022112098003206.
17. Kennel, M. KDTREE 2: Fortran 95 and C++ software to efficiently search for near neighbors in a multi-dimensional Euclidean space. Arxiv preprint physics/0408067. 2004. URL http://arxiv.org/abs/physics/0408067
18. Kleinstreuer C, Li Z, Farber Ma. Fluid-structure interaction analyses of stented abdominal aortic aneurysms. Annual review of biomedical engineering. Jan.2007 9:169–204. URL http://www.ncbi.nlm.nih.gov/pubmed/17362195.
19. Lantz J, Karlsson M. Large eddy simulation of LDL surface concentration in a subject specific human aorta. Journal of Biomechanics. 2012; 45(3):537–42. URL http://www.ncbi.nlm.nih.gov/pubmed/22153749. [PubMed: 22153749]
20. Lasheras JC. The Biomechanics of Arterial Aneurysms. Annual Review of Fluid Mechanics. Jan; 2007 39(1):293–319. URL http://www.annualreviews.org/doi/abs/10.1146/annurev.fluid.39.050905.1101.
21. Le, TB.; Sotiropoulos, F. Fluid – structure interaction of an aortic heart valve prosthesis driven by an animated anatomic left ventricle. Journal of Computational Physics. 2012. URL http://dx.doi.org/10.1016/j.jcp.2012.08.036
22. Mark A, Vanwachem B. Derivation and validation of a novel implicit second-order accurate immersed boundary method. Journal of Computational Physics. Jun; 2008 227(13):6660–6680. URL http://linkinghub.elsevier.com/retrieve/pii/S0021999108001770.
23. Mittal R, Dong H, Bozkurttas M, Najjar FM, Vargas A, Von Loebbecke A. A versatile sharp interface immersed boundary method for incompressible flows with complex boundaries. Journal of Computational Physics. 2008; 227(10):4825–4852. URL http://dx.doi.org/10.1016/j.jcp.2008.01.028. [PubMed: 20216919]
24. Mittal R, Iaccarino G. Immersed boundary methods. Annual Review of Fluid Mechanics. 2005; 37(1):239–261. URL http://www.annualreviews.org/doi/pdf/10.1146/annurev.fluid.37.061903.17574.
25. Peskin C, McQueen D. A three-dimensional computational method for blood flow in the heart I. Immersed elastic fibers in a viscous incompressible fluid. Journal of Computational Physics. 1989; 37245:372–405. URL http://www.sciencedirect.com/science/article/pii/0021999189902131.
26. Peskin CS. Flow patterns around heart valves: A numerical method. Journal of Computational Physics. 1972; 10(2):252–271. URL http://dx.doi.org/10.1016/0021-9991(72)90065-4.
27. Peskin CS. The immersed boundary method. Acta Numerica. 2003; 11(1):479–517. URL http://www.journals.cambridge.org/abstract_S0962492902000077.
28. Pinelli A, Naqavi I, Piomelli U, Favier J. Immersed-boundary methods for general finite-diffierence and finite-volume Navier–Stokes solvers. Journal of Computational Physics. Dec; 2010 229(24):9073–9091. URL http://linkinghub.elsevier.com/retrieve/pii/S0021999110004687.

29. Posa A, Lippolis A, Verzicco R, Balaras E. Large-eddy simulations in mixed-flow pumps using an immersed-boundary method. Computers & Fluids. Aug; 2011 47(1):33–43. URL http://linkinghub.elsevier.com/retrieve/pii/S0045793011000569.
30. Reba I. Applications of the Coanda effect. Scientific American. 1966; 214:84–92.
31. Shadden SC, Taylor Ca. Characterization of coherent structures in the cardiovascular system. Annals of biomedical engineering. Jul; 2008 36(7):1152–62. URL http://www.ncbi.nlm.nih.gov/pubmed/18437573. [PubMed: 18437573]
32. Shetty D, Shen J, Chandy A, Frankel S. A pressure-correction scheme for rotational navier-stokes equations and its application to rotating turbulent flows. 2011
33. Shetty DA, Fisher TC, Chunekar AR, Frankel SH. High-order incompressible large-eddy simulation of fully inhomogeneous turbulent flows. Journal of Computational Physics. Nov; 2010 229(23):8802–8822. URL http://linkinghub.elsevier.com/retrieve/pii/S0021999110004481.
34. Tennekes, H.; Lumley, J. A first course in turbulence. MIT press; 1972.
35. Tylli N, Kaiktsis L, Ineichen B. Sidewall effects in flow over a backward-facing step: Experiments and numerical simulations. Physics of Fluids. 2002; 14(11):3835. URL http://link.aip.org/link/PHFLE6/v14/i11/p3835/s1&Agg=doi.
36. Vanella M, Rabenold P, Balaras E. A direct-forcing embedded-boundary method with adaptive mesh refinement for fluid–structure interaction problems. Journal of Computational Physics. 2010; 229(18):6427–6449. URL http://linkinghub.elsevier.com/retrieve/pii/S002199911000255X.
37. Varghese SS, Frankel SH, Fischer PF. Direct numerical simulation of stenotic flows. Part 1. Steady flow. Journal of Fluid Mechanics. Jun.2007 582:253. URL http://www.journals.cambridge.org/abstract_S0022112007005848.
38. Varghese SS, Frankel SH, Fischer PF. Direct numerical simulation of stenotic flows. Part 2. Pulsatile flow. Jun.2007 582 URL http://www.journals.cambridge.org/abstract_S0022112007005836.
39. Vreman AW. An eddy-viscosity subgrid-scale model for turbulent shear flow: Algebraic theory and applications. Physics of Fluids. 2004; 16(10):3670. URL http://link.aip.org/link/PHFLE6/v16/i10/p3670/s1&Agg=doi.
40. Welch P. The use of fast Fourier transform for the estimation of power spectra: A method based on time averaging over short, modified periodograms. IEEE Transactions on Audio and Electroacoustics. 1967; 15(2):70–73. URL http://ieeexplore.ieee.org/xpls/abs_all.jsp?arnumber=1161901.
41. Wilcox, DC. Turbulence modeling for CFD. 2. DCW Industries; 2000.
42. Wille R, Fernholz H. Report on the first European Mechanics Colloquium, on the Coanda effect. Journal of Fluid Mechanics. 1965; 23(4):801–819.
43. Yokoi K, Xiao F, Liu H, Fukasaku K. Three-dimensional numerical simulation of flows with complex geometries in a regular Cartesian grid and its application to blood flow in cerebral artery with multiple aneurysms. Journal of Computational Physics. Jan; 2005 202(1):1–19. URL http://linkinghub.elsevier.com/retrieve/pii/S0021999104002657.

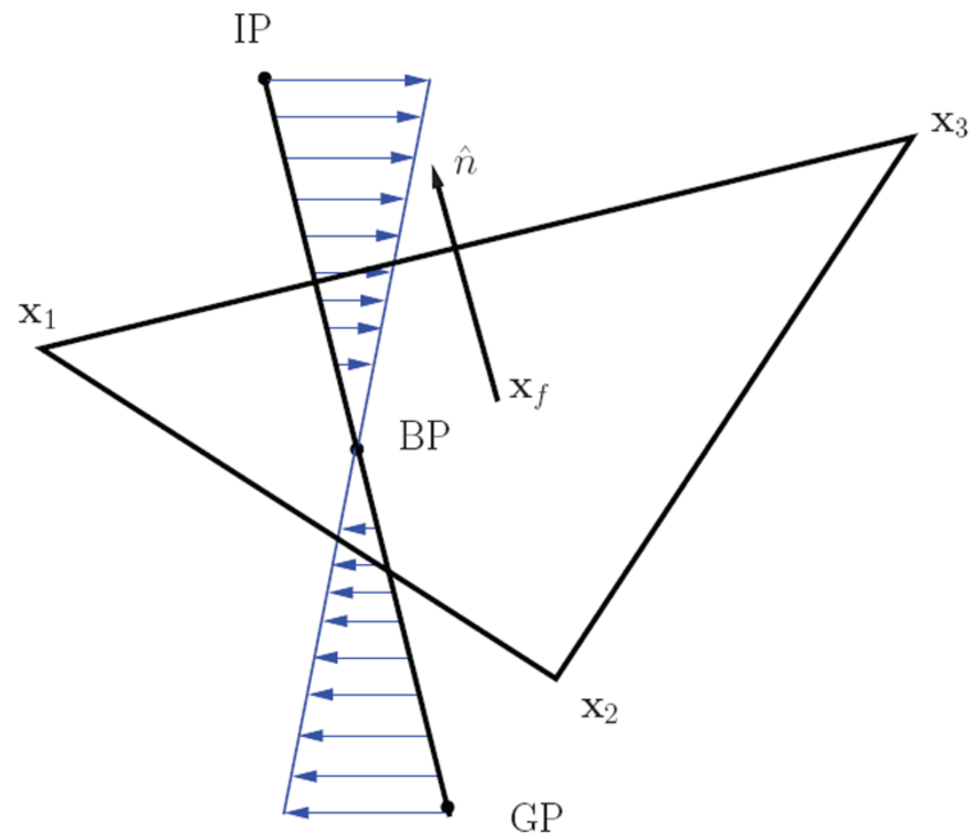

Figure 1.
Schematic of the mirroring immersed boundary method; $\mathbf{x_1}$, $\mathbf{x_2}$, and $\mathbf{x_3}$ are the coordinates of the vertices of the triangles that make up the Lagrangian surface mesh. $\mathbf{x_f}$ is the face centroid and $\hat{n}$ is the face normal vector of the triangle, that always points in the direction of the fluid. *IP, BP* and *GP* are respectively the image point, boundary point and the ghost point.

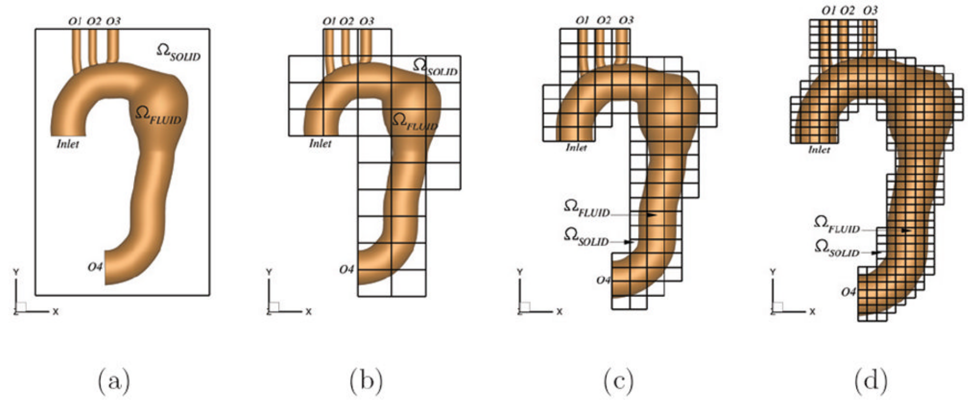

Figure 2.

Geometry of thoracic aortic aneurysm enclosed in a (a) single block domain (SB) (b) multiblock decomposition with 32 blocks (MB1). (c) A multiblock decomposition with 100 blocks (MB2) (d) A multiblock decomposition with 325 blocks (MB3). The surface *Inlet* indicates inflow to the domain and the surfaces $O1$, $O2$, $O3$ and $O4$ indicate the outlets to brachiocephalic artery, left common carotid artery, left subclavian artery and to abdominal aorta respectively. Ω_{FLUID} and Ω_{SOLID} represent the fluid and the solid regions respectively.

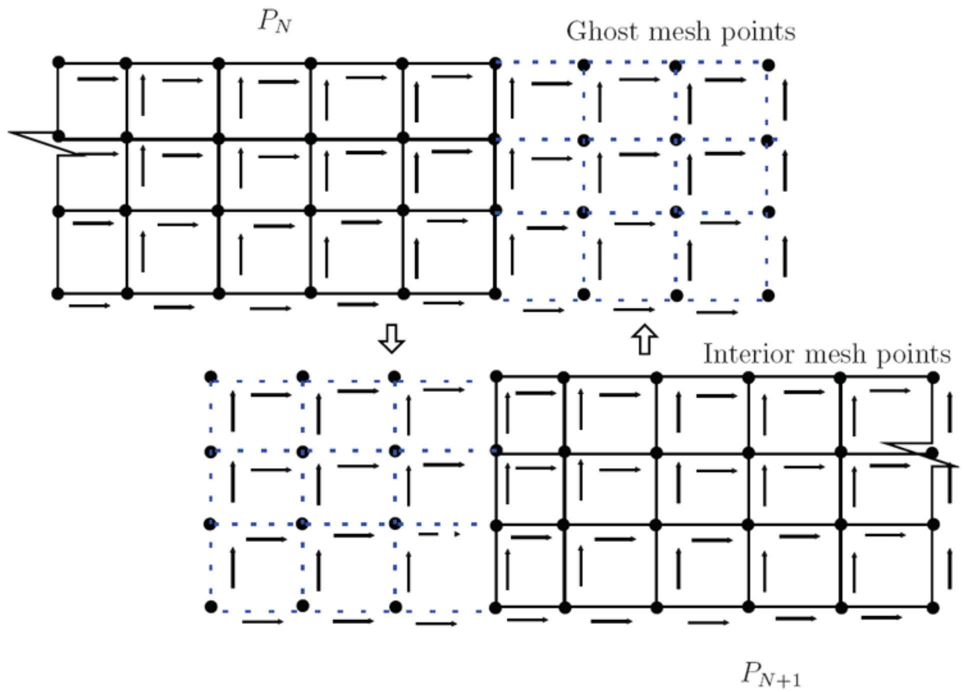

Figure 3.
Two dimensional schematic showing the $1D$ decomposition of the domain in parallel solver. The horizontal arrows indicate the location where u velocity values are stored, vertical arrows indicate the location where v velocity values are stored and the circles indicate the location of pressure (p) points. A sample of three ghost layers of the grid is shown plotted. Labels P_N and P_{N+1} indicate n^{th} and $(n+1)^{th}$ processors respectively in a parallel decomposition.

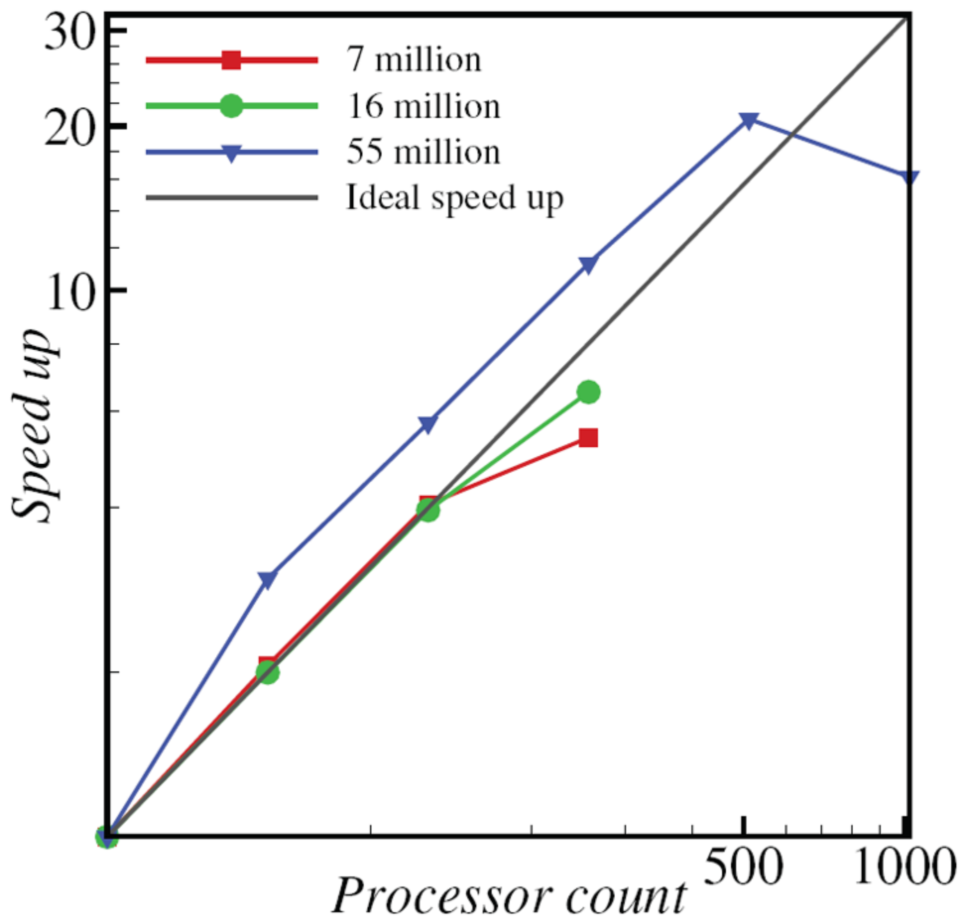

Figure 4.
Parallel performance of the *WenoHemo* solver

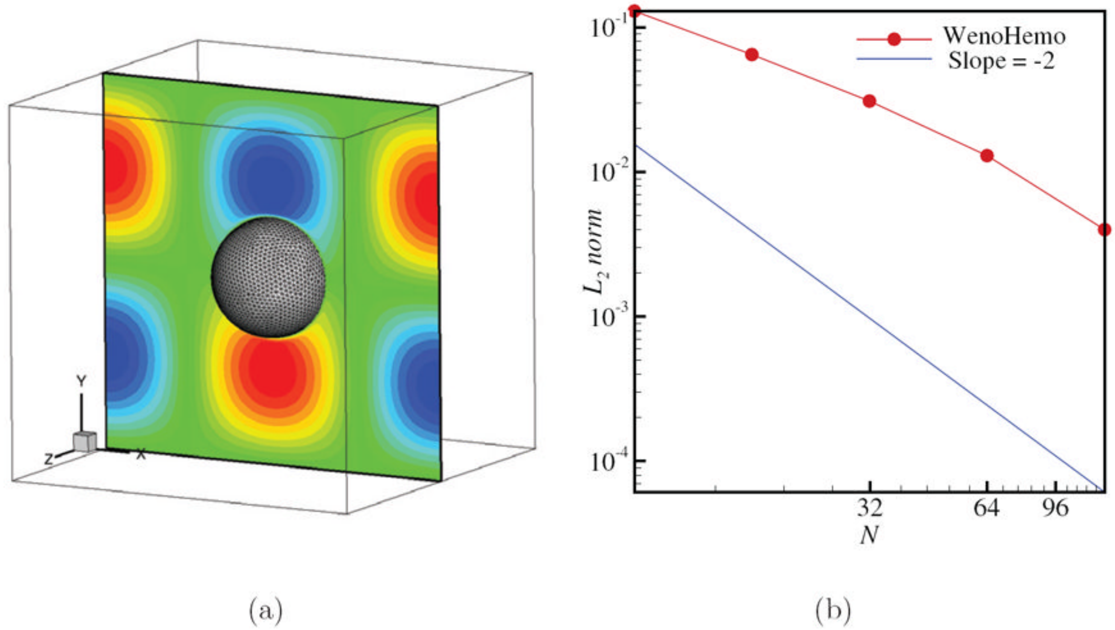

Figure 5.
(a) Contours of u-velocity component on $z = 0$ plane for the grid size of 256^3 (b) Variation of L_2 error norm of the u-component of velocity as a function of the grid size depicting the spatial order of accuracy of the present solver.

NIH-PA Author Manuscript

NIH-PA Author Manuscript

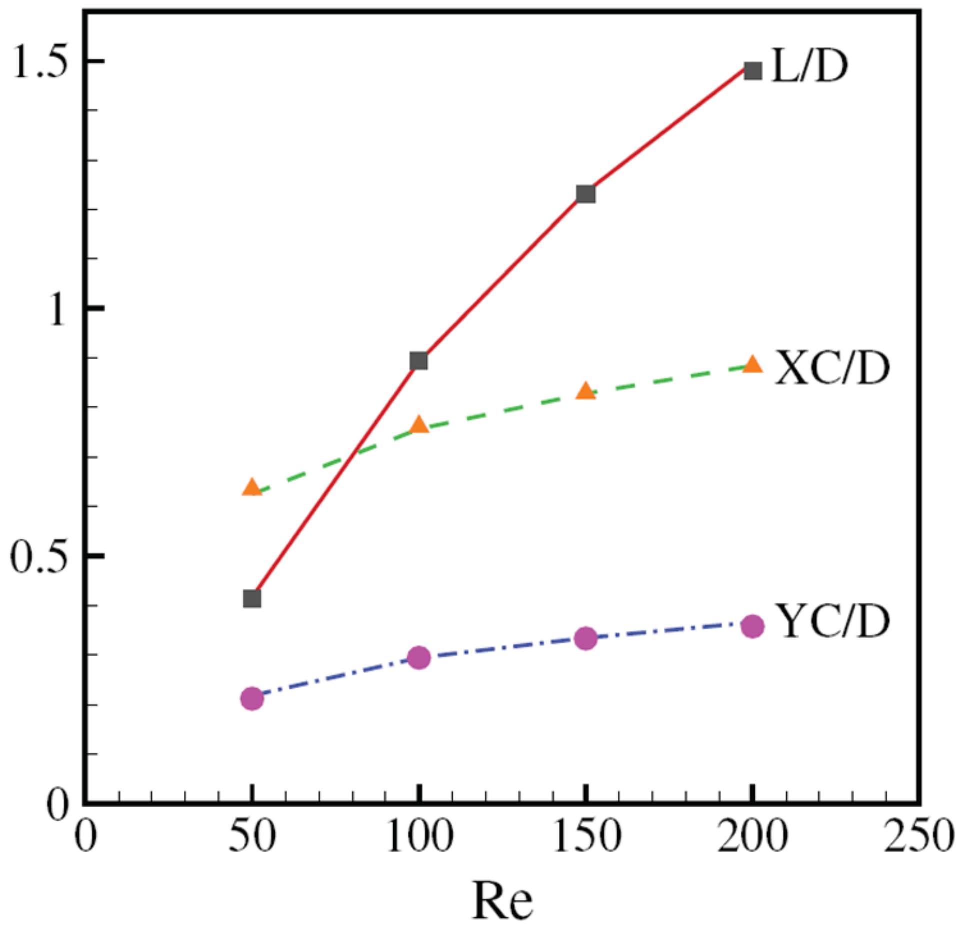

Figure 6.
Comparison of separation bubble parameters to the results of Johnson et al. [16]; lines denote the present computations with *WenoHemo* solver, symbols denote the results obtained by Johnson et al. [16]

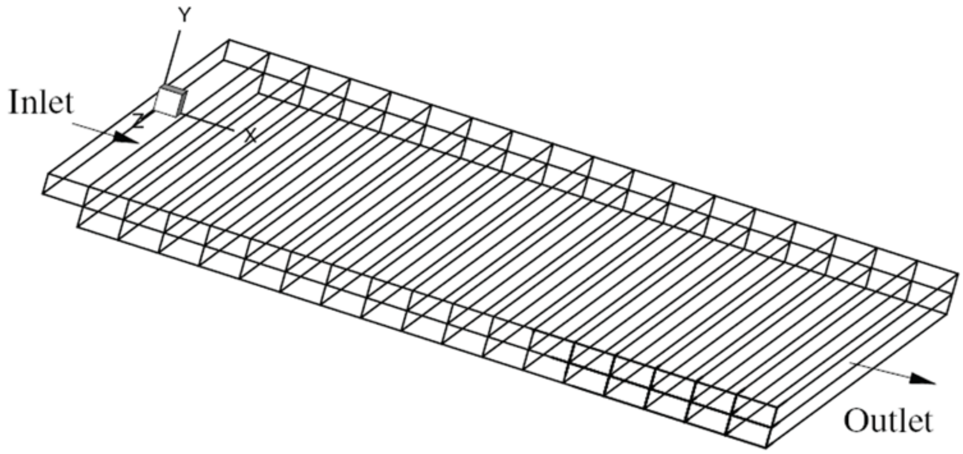

Figure 7.
Schematic of the backward facing step geometry used in the present calculations. The decomposition of the domain into 35 equal sized blocks to create the step and and outlet geometry is also depicted.

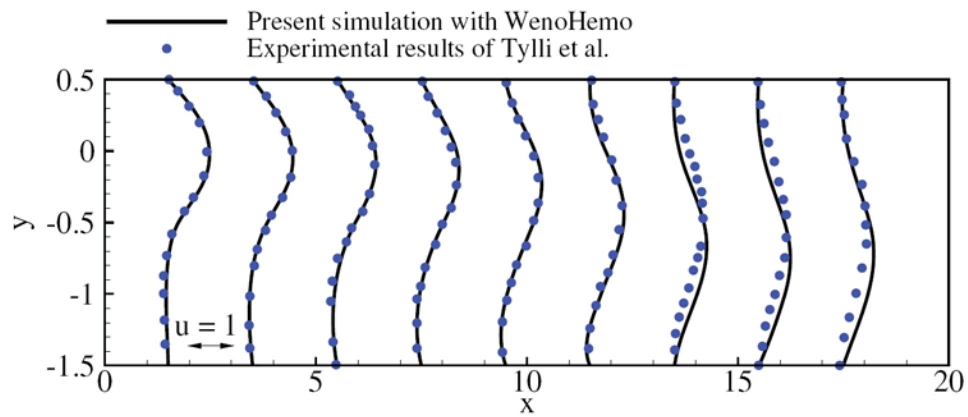

Figure 8.
Re = 648: *u*-velocity profiles vs *y* coordinate, at a number of stream-wise cross sections, for *z* = 0 plane, for experiment and simulation. (The *x* and *y* scales are not same)

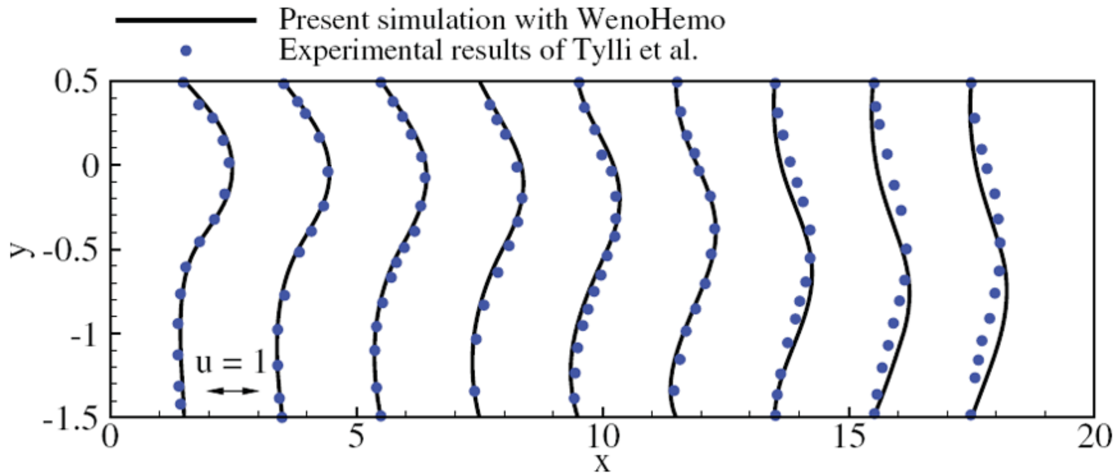

Figure 9.
Re = 648: *u*-velocity profiles vs *y* coordinate, at a number of stream-wise cross sections, for *z* = 10 plane, for experiment and simulation. (The *x* and *y* scales are not same)

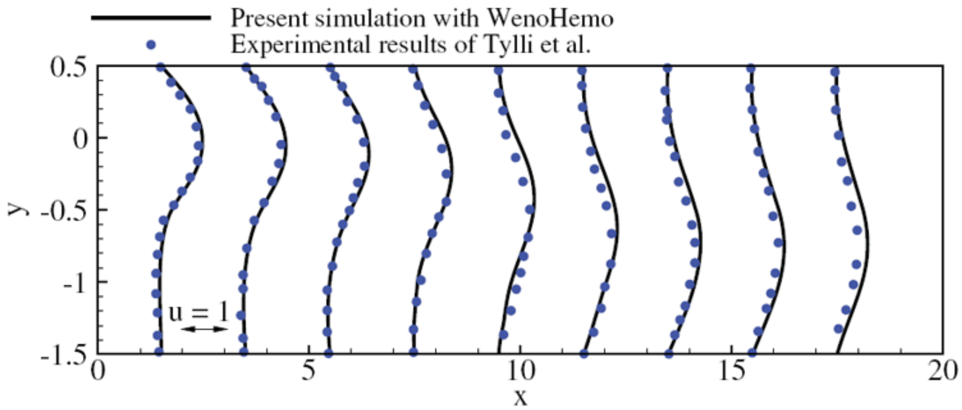

Figure 10.
Re = 648: *u*-velocity profiles vs *y* coordinate, at a number of stream-wise cross sections, for *z* = 18 plane, for experiment and simulation. (The *x* and *y* scales are not same)

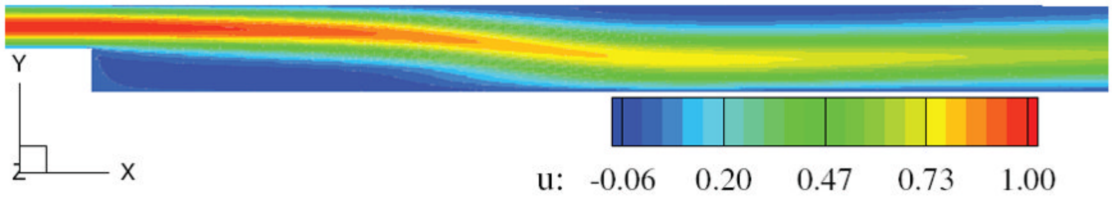

Figure 11.

Re = 648: *u*-velocity contours, for *z* = 0 plane, for simulation

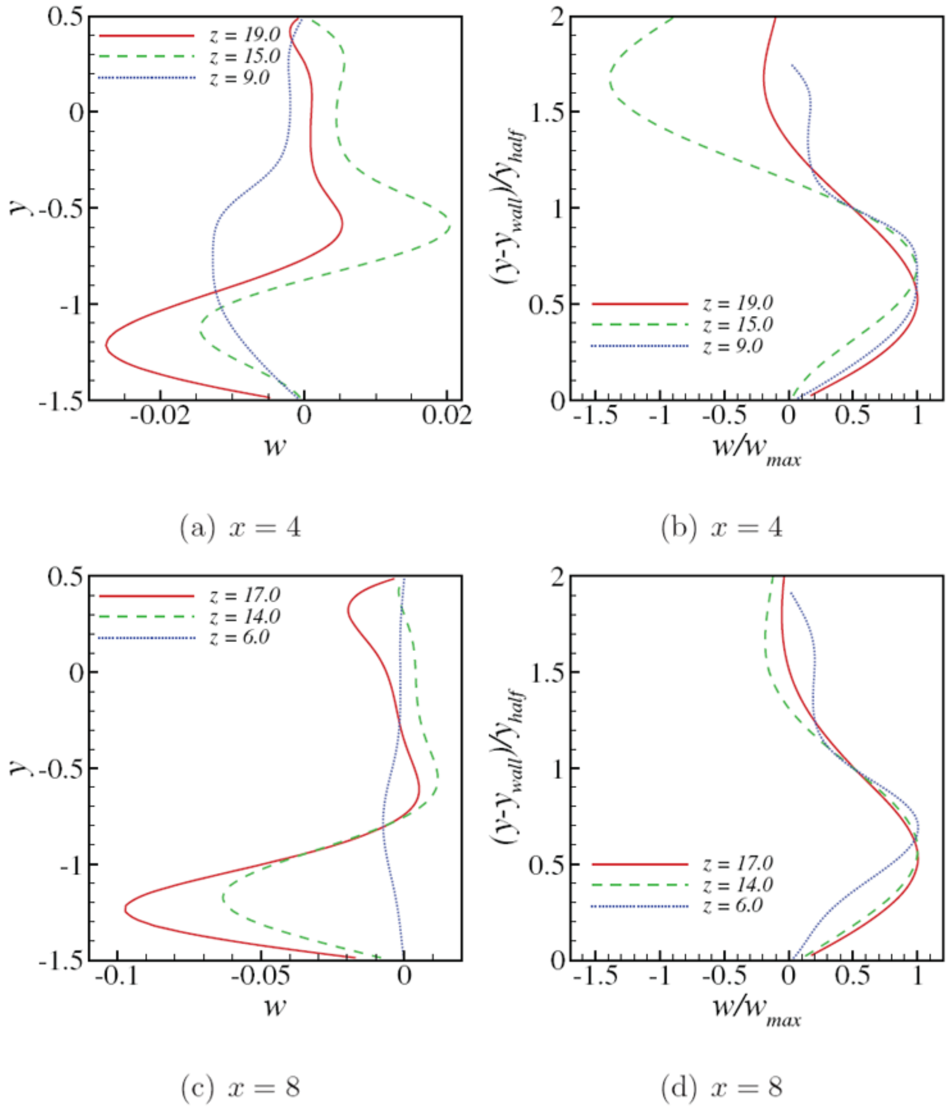

Figure 12.
$Re = 648$: w-velocity profiles: original(left column) and normalized (right column); plotted as a function of y-coordinate at indicated z locations and x planes.

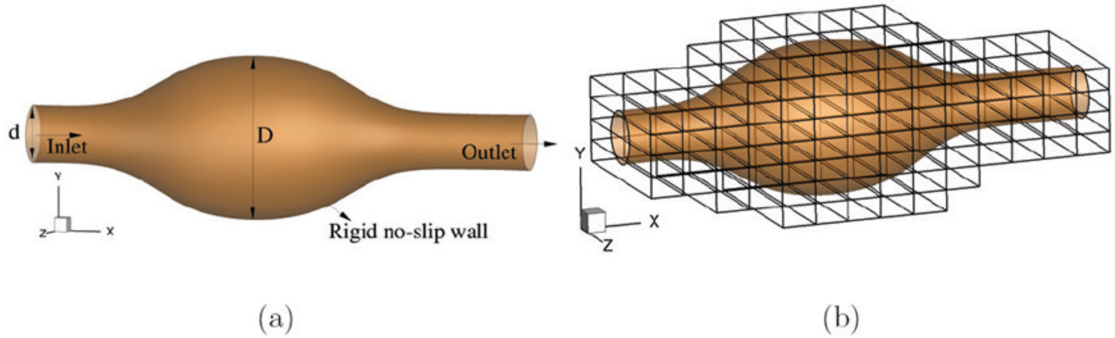

Figure 13.
(a) Geometry of AAA reconstructed from the experiments of Asbury et al. [1]. (b) Multiblock decomposition of AAA into 81 equal sized blocks.

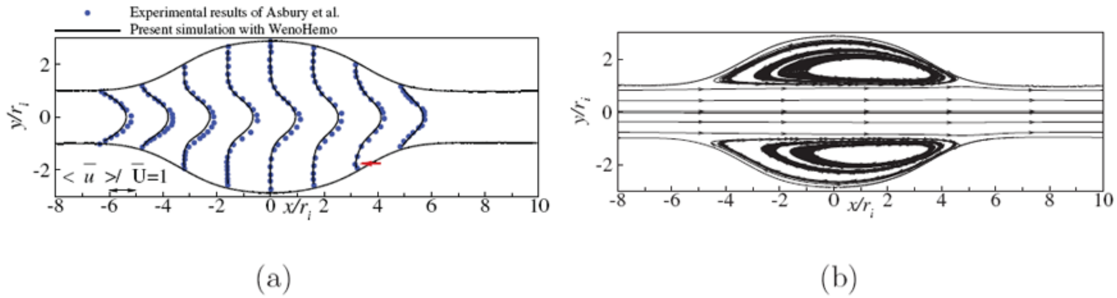

Figure 14.
(a) Comparison of mean axial velocity profiles between present simulations and the experimental results of Asbury et al. [1]. Arrow indicates sample location of retrograde flow close to the wall in the aneurysm region. (b) Streamlines on the *xy*-plane at $z = 0$, depicting the recirculating zone in the aneurysm region.

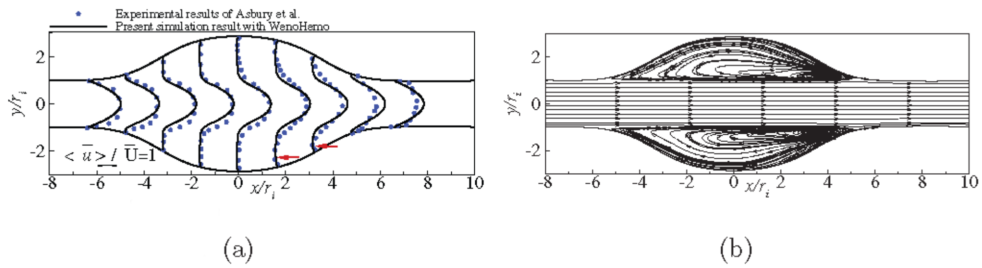

Figure 15.

(a) Comparison of mean axial velocity profiles between present simulations and the experimental results of Asbury et al. [1]. Arrow indicates sample location of retrograde flow close to the wall in the aneurysm region. (b) Streamlines in the *xy*-plane at $z = 0$, depicting the recirculating zone in the aneurysm region.

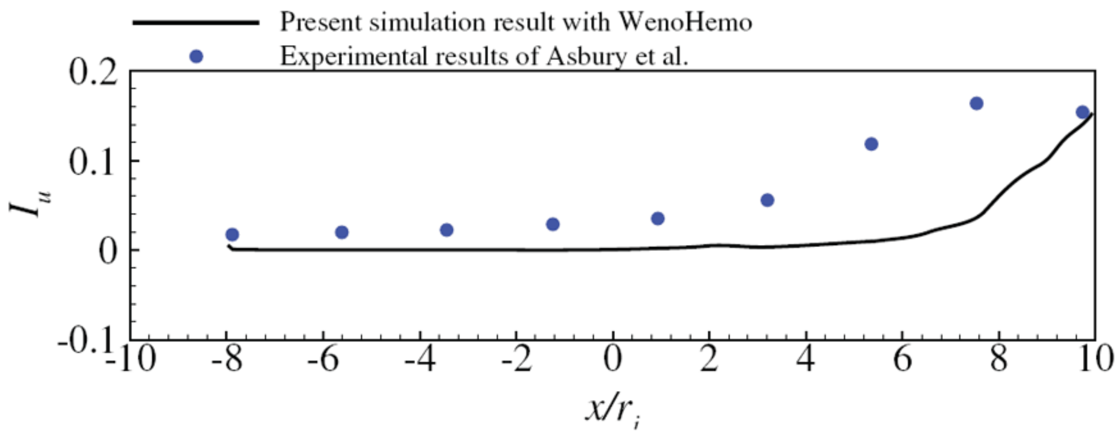

Figure 16.

Comparison of variation of turbulence intensity along the center line of the AAA at a Re = 2600 between simulation and experiment.

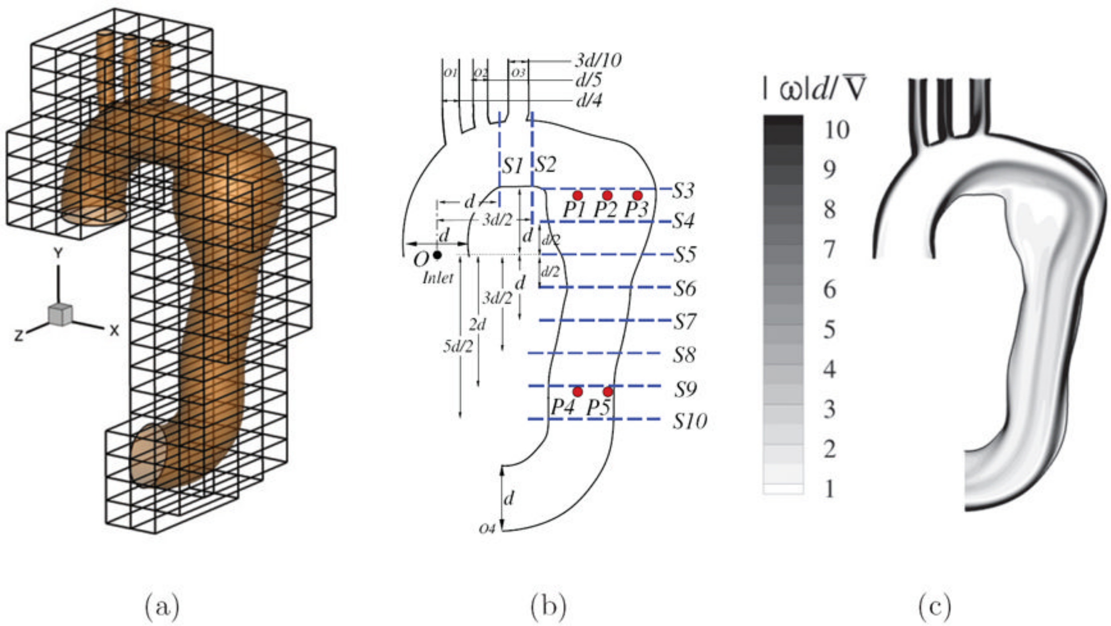

Figure 17.

(a) Decomposition of TAA into 100 multiblocks. (b) Schematic of TAA on the bisecting *xy*-plane at $z = 0$ depicting the sampling lines *S*1 through *S*10 and sampling points *P*1 through *P*5 in the aneurysm and descending aorta regions where data is collected. The coordinates of indicated points are *O*(0, 0), *P*1(2.2*d*, 0.9*d*), *P*2(2.6*d*, 0.9*d*), *P*3(3.1*d*, 0.9*d*), *P*4(2.2*d*, −2.1*d*) and *P*5(2.6*d*, −2.1*d*). (c) Contours of non-dimensional vorticity magnitude ($|\omega| d/\bar{V}$) on the bisecting *xy*-plane at $z = 0$, for steady inflow in TAA at a Reynolds number of 910.

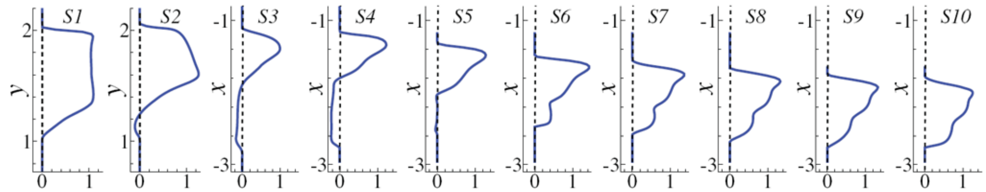

Figure 18.

Mean axial velocity profiles (locations $S1$ and $S2$ show $<\bar{u}>/\bar{V}$, all other locations show $-<\bar{v}>/\bar{V}$) on indicated lines $S1$ through $S10$ for steady inflow in TAA at a Reynolds number of 910.

NIH-PA Author Manuscript
NIH-PA Author Manuscript

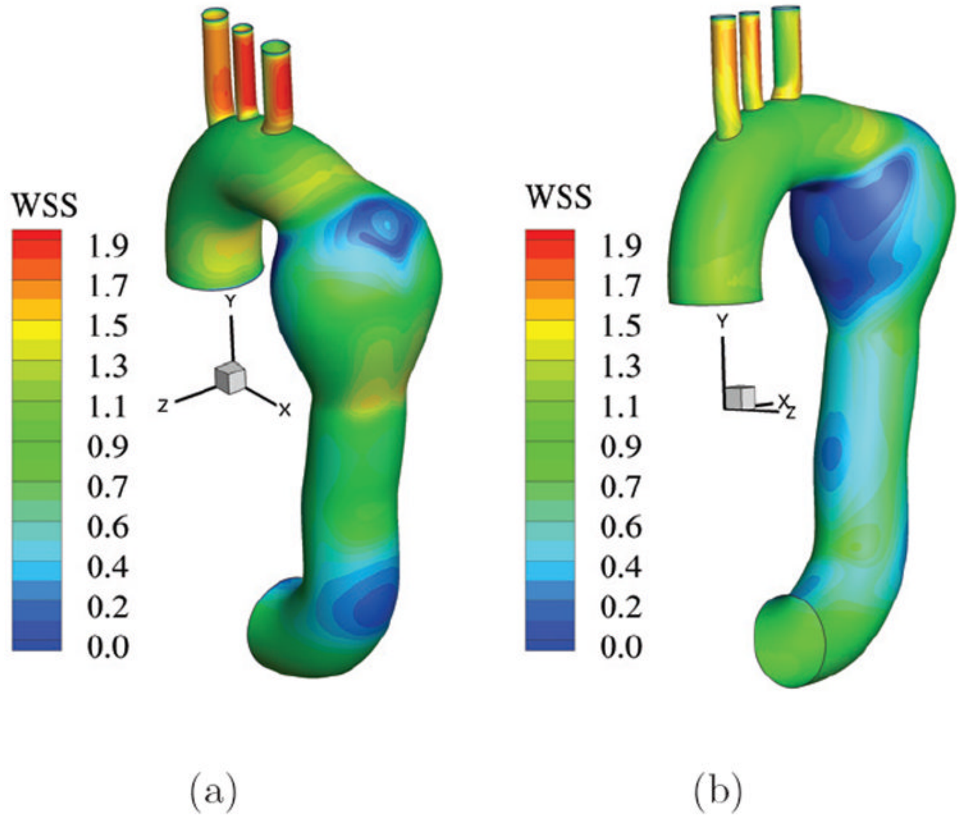

Figure 19.

Contours of normalized mean WSS for a steady inflow at a Reynolds number of 910. The average WSS at the inlet is used for normalization. Frames (a) and (b) show the plot from two different views.

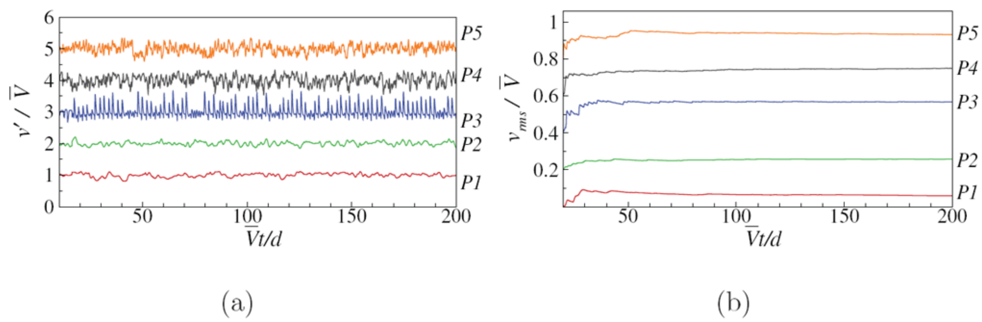

Figure 20.

(a) Time history of $v'/\overline{V}$ at locations $P1$ through $P5$. The $v'/\overline{V}$ value at each station is offset by 1 unit. (b) Time history of $v_{rms}/\overline{V}$ at locations $P1$ through $P5$. The $v_{rms}/\overline{V}$ value at each location is offset by 0.2 units.

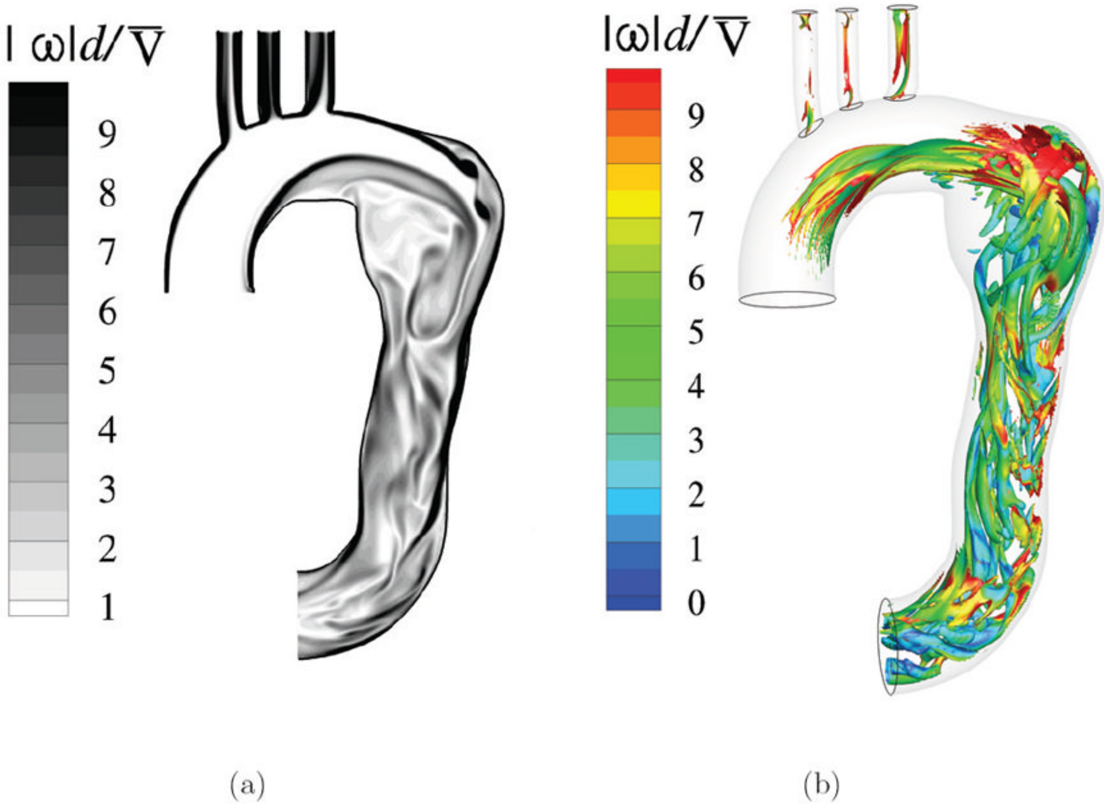

Figure 21.
(a) Instantaneous contours of non-dimensional vorticity magnitude on the bisecting *xy*-plane, at $z = 0$. (b) Instantaneous iso-surface of $\lambda_2 = -2.0$ colored by non-dimensional vorticity magnitude

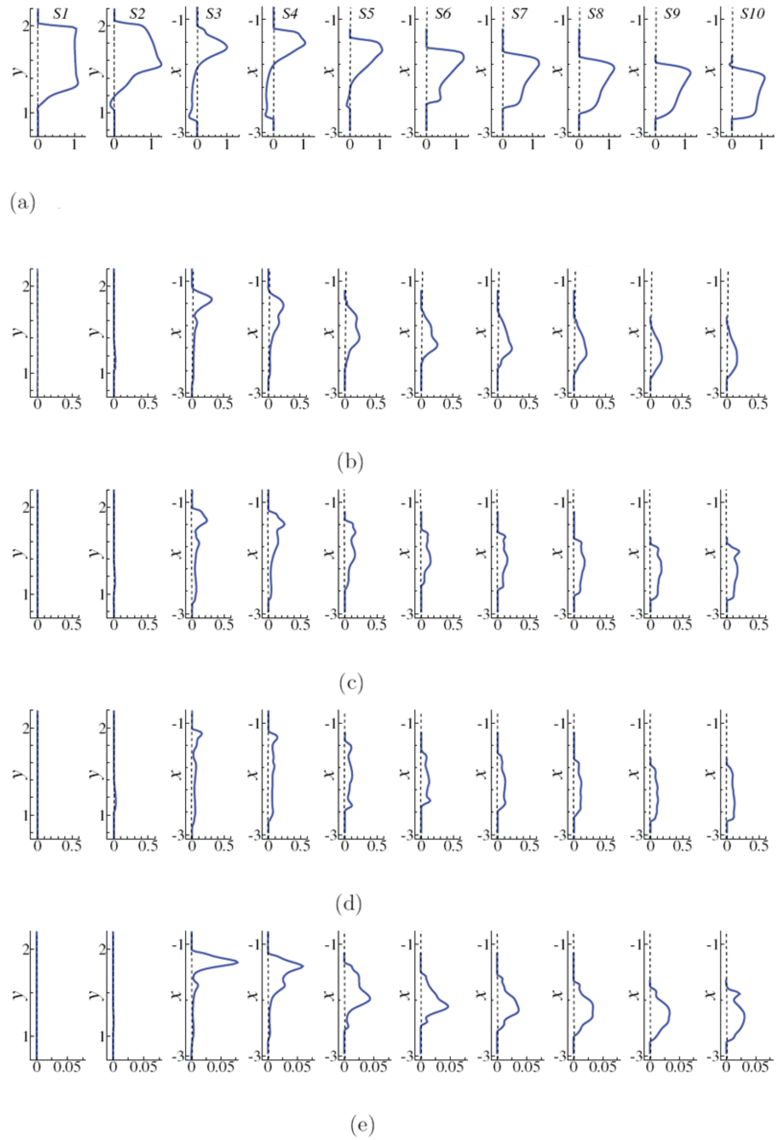

Figure 22.

Steady inflow in TAA at a Reynolds number of 3727. (a) Mean axial velocity profiles (locations $S1$ and $S2$ show $<\bar{u}>/V$, all other locations show $-<\bar{v}>/V$) (b) u_{rms}/V profiles (c) v_{rms}/V profiles (d) w_{rms}/V profiles (e) Normalized turbulent kinetic energy (k/V^2) profiles on indicated lines $S1$ through $S10$.

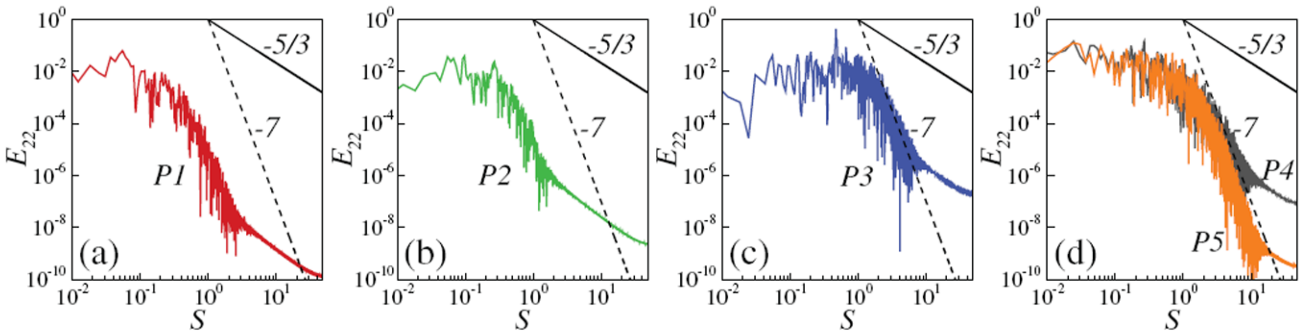

Figure 23.
Frequency spectra corresponding to the velocity fluctuations (v'). The letter adjacent to each of the curves identifies the point where the signal is measured. The solid and the dashed straight lines correspond to $S^{-5/3}$ and S^{-7} respectively as marked. (a) Spectra at location $P1$ (b) Spectra at location $P2$ (c) Spectra at location $P3$ (d) Spectra at locations $P4$ and $P5$. The locations of the points $P1$ through $P5$ are shown in Figure 17(b)

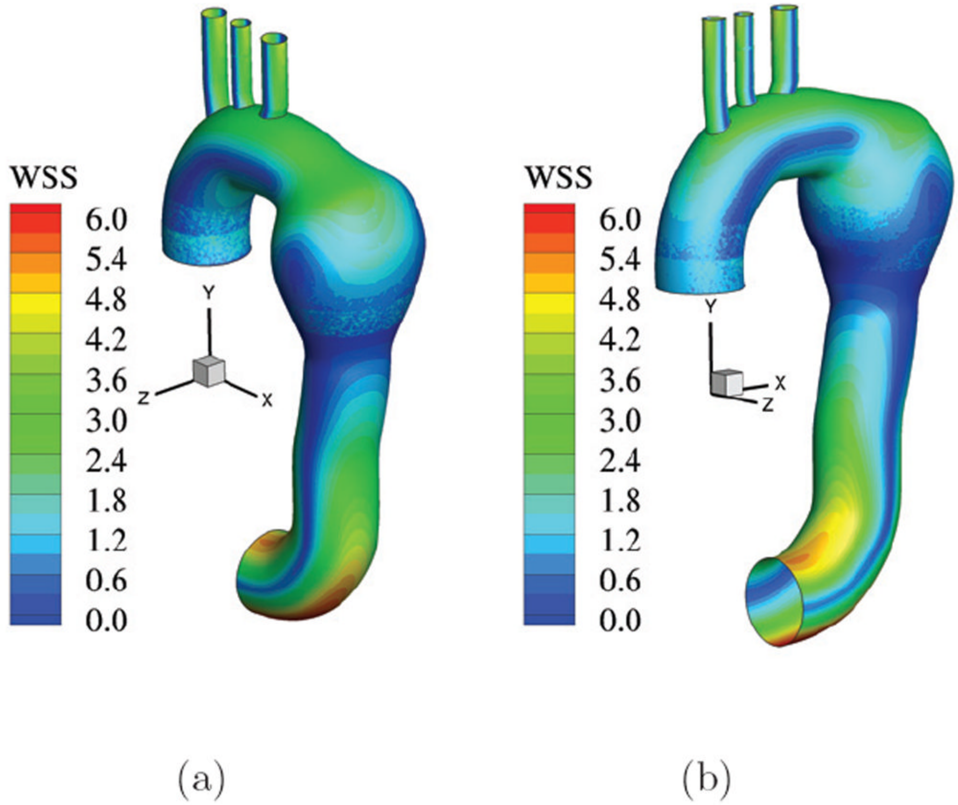

Figure 24.
Contours of normalized mean wall shear stress (WSS) for a steady inflow at a Reynolds number of 3727. The average wall shear stress at the inlet is used for normalization. Frames (a) and (b) show the plot from two different views.

Table 1

Description of several block arrangements and the corresponding Volume Ratio (VR) values that maintains the same grid size in each direction by enclosing the entire fluid domain to be simulated.

Case	SB	MB1	MB2	MB3
No. of blocks	1	31	100	325
Grid points/block	400 × 800 × 80	80 × 80 × 80	40 × 40 × 80	20 × 20 × 80
Total grid points	25, 600, 000	15, 872, 000	12, 800, 000	10, 400, 000
Volume Ratio (VR)	100%	62%	50%	40%